# FINITE ELEMENT SIMULATION OF THE MRTA TEST OF A HUMAN TIBIA

by

Jared George Ragone

Thesis submitted to the Faculty of the Virginia Polytechnic Institute and State University in partial fulfillment of the requirements for the degree of

MASTER OF SCIENCE

In

Biomedical Engineering and Sciences (BMES)

John Cotton, Chair
James Carneal
William Herbert

Wednesday, April 12th, 2006
Blacksburg, Virginia

Keywords: MRTA, finite element modeling, tibia, vibration

# FINITE ELEMENT SIMULATION OF THE MRTA TEST
# OF A HUMAN TIBIA

by
Jared George Ragone
Committee Chair: John Cotton
Biomedical Engineering and Sciences (BMES)

## Abstract

The mechanical response tissue analyzer (MRTA) tests long bone quality through low frequency, low amplitude vibration *in vivo*. The MRTA measures complex stiffness over a range of low frequencies, offering a wealth of information on bone composition. Previous MRTA interpretation used lumped parameter algorithms focused on reliably estimating the bone's bending stiffness (EI). To interpret the stiffness response, the first finite element (FE) simulation of the MRTA test of a human tibia was developed to identify dominant parameters that will possibly make linear prediction algorithms more suitable for estimating bone quality.

Five FE models were developed in stages by adding complexity. Starting with a solid mesh of the diaphysis, each model was created from its predecessor by sequentially adding: a medullary canal, linear elastic (LE) cancellous epiphyses, linear viscoelastic (LVE) cancellous and cortical bone, and a LVE skin layer. The models were simulated in vibration using a direct steady-state dynamics procedure in ABAQUS to calculate the complex stiffness response.

Natural frequency analysis (ABAQUS) verified that the FE models accurately reproduced previous experimental and computational resonances for human tibiae. A solid, LE cortex roughly matched the dominant frequency from experimental MRTA raw data. Adding the medullary canal and LVE properties to bone did not greatly spread the

peak or shift the resonant frequency. Adding the skin layer broadened the peak response to better match the MRTA experimental response. These results demonstrate a simulation of the MRTA response based upon published geometries and material data that captures the essence of the instrument.

# Acknowledgements

I would like to sincerely thank Dr. Herbert and Dr. Carneal for serving as members of my committee and contributing to the overall progress of this thesis. Most importantly, I would like to thank my advisor, committee chairman, and friend, Dr. Cotton. His unyielding support, patience, and outgoingness have greatly contributed to the completion of this thesis.

I would additionally like to thank Chris Callaghan and Larry Miller for providing the necessary background information and experimental data for the MRTA. I would also like to thank my loving family, friends, and beautiful fiancée, Megan, for their support during the completion of this work.

# Table of Contents

# List of Figures

# List of Tables

# List of Equations

# 1. Introduction

Mechanical response tissue analysis (MRTA), which was developed to monitor bone integrity, is an inexpensive and portable device that measures the stiffness of long bones through low frequency, low amplitude vibration. The MRTA experimental technique measures the complex frequency response and estimates the average cross sectional bending stiffness (EI) along the length of the bone being tested. Numerous research studies have investigated the clinical capability and reliability of MRTA EI values, concluding that:

- MRTA EI values of the human ulna correlated with bone mineral content measured by dual energy x-ray absorptiometry (DEXA) ($R^2$=0.81) and showed good reliability with coefficients of variation (COV) on the order of 3-5% (Steele, 1988).
- The MRTA technology differentiated between ulnar EI values of stronger, more athletic subjects and age matched subjects of lower habitual exercise levels (Myburgh, 1993).
- MRTA was effective in distinguishing the stronger (higher EI) tibiae and ulnas of gymnasts and swimmers from the lower EI values for an untrained group (Liang, 2005).
- The MRTA stiffness values for the human tibia showed a very high correlation ($R^2$=0.95) with tibial stiffness values from experimental three-point bending tests (Roberts, 1996).

These findings suggest that the MRTA is an acceptable measurement tool for monitoring bone quality and evaluating the level of strength (EI) for the ulna and the tibia. Since EI is a good predictor of fracture risk (Roberts, 1996), the ability to assess ulnar and tibial EI gives confirmation that the MRTA may be suitable for clinical prediction of fracture risk in humans. The MRTA, however, has been problematic in human tibia strength assessments due to poor repeatability. Coefficients of variation as high as 36% have been reported for long-term measurements for tibial strength (Callaghan, 2003). Since these high variations in the measurements are not fully understood, the hardware and software of the MRTA have limitations, which have hindered future clinical use for the device.

Currently, the interpretation of experimental MRTA raw data is based on lumped parameter models that attempt to curve fit this data. These lumped parameters, shown in Figure 1.1, assume linear stiffness and damping coefficients for the bone, soft tissue, and proximal and distal end conditions. However, the overall dynamic damping response of bone may not be correctly assumed by a single damping parameter. Therefore, these lumped parameter components may incorrectly represent their anatomical counterparts, and this inaccuracy may be a direct cause of the poor reliability associated the MRTA tibial strength assessments.

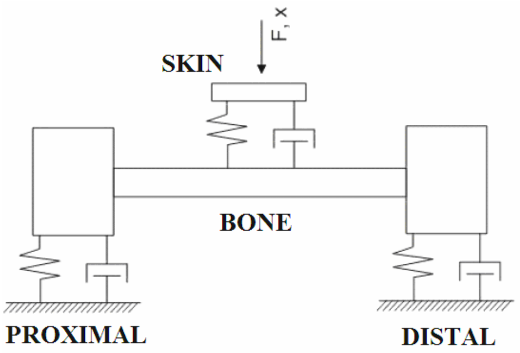

**Figure 1.1: 12-parameter MRTA model for the tibia (reproduced with permission: Steele, 2006)**

This thesis presents the first finite element (FE) simulation of the MRTA test of a human tibia. The complex stiffness versus frequency calculated by the MRTA offers a wealth of information on the material and structural composition of the bone being tested; however, previous interpretation of the MRTA has only focused on reliably determining EI. This thesis applies several distributed parameter FE models to interpret the complex stiffness response of the tibia under vibration. The ultimate goal of the FE simulation is to determine:

1) Accurate lumped parameter models for determining the EI of the tibia
2) The ability of MRTA to estimate other parameters of interest to bone integrity such as damping.

The distributed FE models provide a systematic method to examine which parameters dominate the stiffness response of the human tibia in vibration. The effects of different geometries, material properties, and constraints for the tibia were investigated to observe which parameter was dominant in the frequency domain. The distributed FE model, as shown in Figure 1.2, provides a unique engineering tool to manipulate aspects (damping, geometry, etc.) of the tibia and possibly single out specific limitations associated with the lumped parameter components.

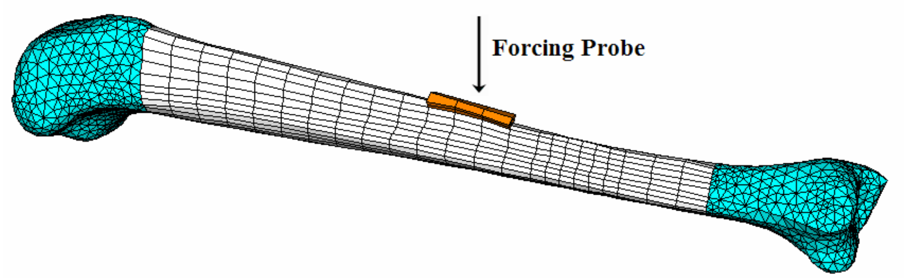

**Figure 1.2: Distributed parameter FE model for a human tibia**

The proposed FE simulation also serves as the groundwork for a “virtual prototype system” for assessing tibial strength. If the proposed methodology accurately predicts the experimental MRTA raw data, the FE simulation technique could be combined with peripheral quantitative computed tomography (pQCT) scans of the human tibia. pQCT uses high ionization energy to generate three-dimensional images of localized bone regions, which can be converted into subject-specific FE tibia models using specialized software. The FE procedures in this thesis could be then applied to the subject-specific FE tibiae to simulate the dynamic stiffness response. Normal (healthy) tibia responses would serve as reference curves in comparison to subject-specific tibiae with abnormal (insufficient) characteristics to better predict fracture risk. Ultimately, this “virtual prototype system” would be an enhanced tool for characterizing long bone strength using diagnostic and dynamic simulation procedures. However, the scope of this thesis is to present the first FE simulations of the MRTA and compare complex stiffness versus frequency responses for the distributed parameter FE models and the experimental MRTA raw data from a tibial strength assessment.

This chapter begins with an overview of the clinical and economical significance for evaluating bone strength and predicting fracture risk (Section 1.1). Section 1.2 presents a brief review of bone composition, remodeling characteristics, bone mechanics, and factors that affect bone properties. Lastly, this chapter concludes with an introduction to the MRTA measurement technology (Section 1.4) and current clinical modalities (Section 1.3) that attempt to evaluate bone integrity.

## 1.1 Significance

Bone is a connective tissue that has several vital physiological functions, including structural support, protection of organs, regulation of calcium, and movement (i.e. attachment for muscles, tendons, and ligaments). Due to these functions, there is a significant need to qualitatively and quantitatively monitor these functions over time so that normal physiological conditions are preserved. To monitor bone functions, the physical, chemical, and mechanical properties of bone are evaluated and tested through various experimental and clinical procedures. Understanding and monitoring these properties has provided significant information for the prediction, diagnosis, and treatment of bone pathologies and fractures.

When physiological or external conditions exceed a certain threshold, the structural integrity of bone can fail leading to different types of fracture, including osteoporotic, traumatic, and stress fractures. These types of fractures, which affect millions of people in the U.S. per year, all induce pain and discomfort, while osteoporotic fractures can reduce the quality of life and increase risk of mortality. Traumatic fractures usually occur during some high loading event such as a car crash or a fall, whereas stress fractures occur in healthy people who exceed their load-carrying capacity of particular bones through repetitive exercise or tasks. Stress fractures are either fatigue fractures in which the fracture occurs in normal bone or insufficiency fractures, where the fracture occurs in bones with reduced mineralization and elasticity (Weber, 1993). Stress fractures affect athletes and military recruits, and raise costs for their respective organizations during lost participation time (Callaghan, 2003).

Osteoporosis is the most common bone disease in the United States, affecting over 10 million people with more than 1.5 million osteoporosis-related fractures per year (Orsini, 2005). The economic impact of these fractures is immense with an estimated $17 billion in health care costs and lost productivity (Munch and Shapiro, 2006). These numbers will continue to grow as the population continues to get older and live longer. Therefore, bone strength research has focused on developing effective predictive technologies for bone fractures. Better prediction of fracture risk for individuals would assist in clinical treatment and prevention while saving the individual or respective institution millions of dollars in medical costs.

Long range space travel provides another significant application for advanced bone strength tools due to the profound effects low-gravity environments have on bone properties. In 2003, NASA administrator Sean O'Keefe, stated, "The human body is profoundly affected by long duration of space travel…after 6 months it is fairly typical for an astronaut, or cosmonaut, to experience a 10 percent degeneration of bone mass and 30 percent degeneration of muscle mass. So as a consequence we have to understand those affects in order to make long duration of space travel for humans possible (Ask the White House, 2003)." With the emergence of commercially available space flights and collaborative space experiments, identification of the appropriate countermeasures to this bone loss first requires improved tools capable of detecting the mechanical integrity of bone.

## *1.2 Bone Properties*

### 1.2.1 Composition

Bone is a specialized tissue with a unique arrangement of microstructures that offer an optimum mass-to strength ratio. The microstructure organization and excellent mass-to strength ratio give bone its excellent mechanical and structural properties that are needed for numerous functions of the human body. Bone's composition and structure, however, both vary in a way that depends on skeletal location, physiological function, age, sex, and environmental factors (Bonucci, 2000). The fundamental components of bone are the organic matrix and the mineral substance. The organic matrix mostly consists of type I collagen fibrils, which account for over 90% of the whole matrix, and the remaining 10% corresponds to noncollagenous proteins, phosholipids, and proteoglycans (Glimcher, 1976). The mineral substance of bone is a calcium phosphate hydroxyapatite, which usually takes the form of microscopic crystals (Posner, 1987).

The human tibia, an irregular-shaped, tubular whole bone, is the load bearing structure in the lower leg. The tibia has three separate segments including a diaphysis or long central shaft, two epiphysis regions at the ends, and two metaphysis regions that represent the transition area between diaphysis and epiphysis ends. Generally, long bones, shown in Figure 1.3, consist of an outer cortical shell and an inner zone called the medullary canal. The macrostructure of the tibia, as illustrated in Figure 1.3, consists of two types of bone, cortical (compact) and cancellous (spongy). Cancellous bone, also called trabecular bone, is characterized by large pores within a network of rod-like or sheet-like microstructures known as trabeculae. The difference between cortical and cancellous bone depends on the level of porosity with a 5-30% range for cortical bone and a range of 30 to 90% for cancellous bone (Bonucci, 2000).

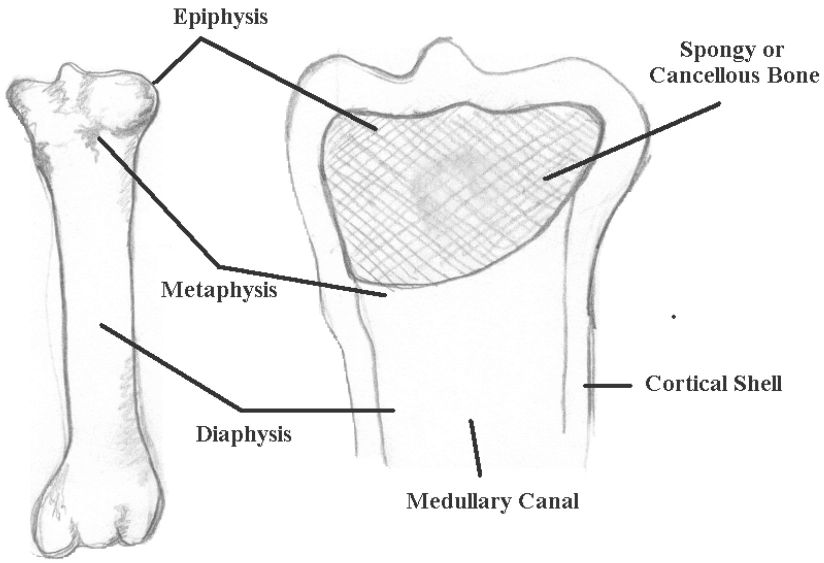

**Figure 1.3: Typical long bone structure and composition**

### 1.2.2 Adaptation

The response of bone to a short-term or long-term loading is directly related to its material composition, distribution, and geometry. This response is characterized by Wolff's Law that states as the function of a bone changes, the internal architecture and external confirmation will adapt to reflect the new function (Wolff, 1986). These functional changes exist due to the complex remodeling process of bone which involves the continual resorption and formation of calcified tissue. Due to cyclic loading over long time periods, bone is continuously put under strain, which causes fatigue microdamage (Burr, 2002). This fatigue microdamage weakens bone and causes cracks, which will accumulate over time and initiate the remodeling characteristics of bone. Bone remodeling will add more bone material during increased loading, and will reduce bone mass during decreased loading. This remodeling of bone structure is based on interactions between osteoblasts or “bone building” osteocytes and osteoclasts or “bone destroying” osteocytes. During bone modeling, the interactions of osteoblasts and osteoclasts continue in a way that favors optimum bone mass and trabecular orientation.

### 1.2.3 Mechanics

In terms of biomechanics, bone is viscoelastic or exhibits time-dependent material behavior. The stiff hydroxyapatite crystals in bone contribute to overall stiffness of bone, whereas the pliant collagen fibers have linear viscoelastic characteristics (Sasaki, 2000). The viscoelasticity of bone refers to its mechanical properties depending considerably upon the rate at which it is deformed. Appendix A provides a review of LVE material behavior and lists experimental viscoelastic parameters for cancellous and cortical bone, which were taken from the literature. Furthermore, bone is anisotropic, which means there is a strong dependency of its mechanical properties on the direction at which forces are applied or strain measurements are taken. The stiffness and arrangement of collagen fibers and hydroxyapatite crystals in cortical and cancellous tissue define bone anisotropy and cause the mechanical stiffness of bone to respond differently according to different directions of loading.

Long bones, which are generally approximated as beams, are subjected to axial and bending forces *in vivo* due to the curvature of the bone. Experimentally, three-point bending loads, shown in Figure 1.4, are applied and generate tensile forces on the convex surface of the bone and compressive forces on the concave surface. The lateral bending stiffness can be estimated using Equation 1.1 by assuming a uniform Euler-Bernoulli beam representation for the bone under simply-supported boundary conditions. The elastic or Young's modulus, *E*, can be coupled with the cross-sectional moment of inertia, *I*, to give the cross-sectional bending stiffness, *EI*. *EI*, shown in Equation 1.2, is calculated from the lateral bending stiffness, which can be experimentally determined using three-point bending tests.

$$\begin{aligned} &k = \frac{48\,EI}{L^3} \qquad \textit{where} \\ &L \textit{ is the distance between supports} \\ &E \textit{ is the elastic modulus of the material} \\ &I \textit{ is the cross sectional moment of inertia} \end{aligned} \qquad \textbf{(1.1)}$$

$$EI = \frac{kL^3}{48} \qquad \textbf{(1.2)}$$

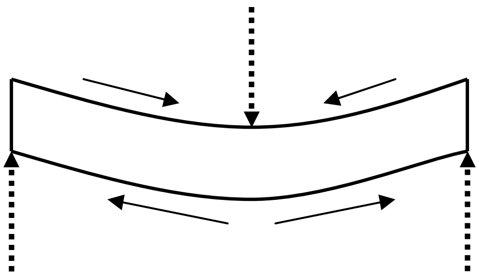

**Figure 1.4: Three-point bending loads on bone (represented as a beam)**

Since the tibia is non-homogenous with irregular geometry, the cross sectional moment of inertia, *I*, is dependent on the cross sectional shape and distribution of bone mass within the cross section. In addition, the elastic or Young's modulus, *E*, is dependent on the orientation, composition, and stiffness of bone constituents, and both *E* and *I* can change along the length of the tibia. For instance, the cross sectional thickness of the tibia at the midshaft, shown in Figure 1.5, has areas of varying bone deposition. At another cross section, this distribution of material would change around the bending axis, and so on. Therefore, the cross sectional moment of inertia would be a function, *I(x)*, where *x* is the distance along the length of the tibia. In addition, the elastic modulus would change along the length of the tibia, and would vary directionally due to the anisotropy of the bone constituents. Therefore, the elastic modulus would be a function, *E(x,y,z)*. The varying thickness of the cortical shell along the length of the tibia significantly affects both the cross sectional moment of inertia, *I*, and elastic modulus, *E*, which in return, directly affect the lateral bending stiffness.

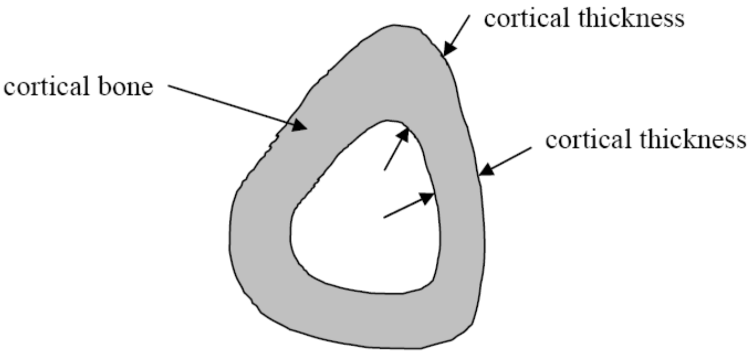

**Figure 1.5: Tibia cross sectional area showing material distribution (reproduced with permission: Callaghan, 2003)**

Since *I* and *E* change for different cross sections, *EI* also varies along the length of the tibia. Therefore, *EI* is often a "weighted" average of stiffness values along the length of the long bone. For example, the MRTA repeats a series of measurements at the midshaft to get average values for the lateral bending stiffness, *k*. These average values for *k* are plugged into Equation 1.2 to estimate the average cross sectional bending. Since *I* depends on the geometry of the cross section and *E* depends on the mechanical properties of bone constituents, *EI* is a measure the bone's mechanical integrity.

### 1.2.4 Factors that Influence Bone Strength

The purpose of mechanical testing of long bones is to characterize the range of normal mechanical properties and to define abnormalities according to those normal values. Bone’s mechanical behavior, however, is a function of the individual properties of collagen and hydroxyapatite, their degree of association and cohesion, the size and shape of these substructures, and their orientation (Zioupos, 2000). Therefore, factors that affect these constituents and their level of association directly influence the strength of bone.

The influence of age on bone is a continuous process with maturation occurring around 35 years of age. At some point in the aging process, the relationship between osteoblast deposition and osteoclast resorption becomes uneven. Cancellous bone begins to fragment causing bone mineral content to decrease, and in return, the mechanical properties of bone begin to deteriorate. Eventually there is a significant loss of cortical and cancellous bone, which has been shown to begin earlier in women and dramatically increases at menopause (Seeman, 2002). Due to the reduction in cortical and cancellous bone mass with age, the load carrying capacity for long bones diminishes and increases susceptibility for fracture.

Physical activity has a direct effect on bone properties due to the physiological response of bone to external loads based on Wolff’s Law. When an individual’s activity level changes, the daily loading strongly influences the resorption and deposition of the cortical bone that is directly experiencing the loading (Currey, 1984). An increase in loading leads to an increase in bone mass and decreased loading leads to a reduction in bone mass. However, an increase in bone mass in adults has shown to only continue as long as the particular activity level is retained (Zioupos, 2000).

Weightlessness and reduced gravity have a major effect on the bone strength because they significantly reduce the daily strain patterns experienced by the bones and thus affect the remodeling process. In this current era of collaborative space missions and asperations to visit Mars, astronauts will be staying longer in space increasing their risk of bone mass loss, especially in weight-bearing bones. Tibial bone mineral density has been shown to decrease during 2-6 months of spaceflight, and the time needed to recover the losses is generally greater than the mission duration (Oganov, 1992).

## *1.3 Current Modalities*

The goal of bone strength research is to develop innovative and precise measurement tools to monitor bone integrity. These measurement tools attempt to accurately quantify normal and abnormal bone quality for the purpose of identifying individuals at risk for fractures. Currently, several techniques have been utilized to predict the strength of bones with varying levels of success. This section introduces and discusses the advantages and disadvantages of three bone strength technologies: dual-energy x-ray absorptiometry (DEXA), quantitative computed tomography (QCT), and quantitative ultrasound (QUS) methods.

### 1.3.1 Dual-Energy X-Ray Absorptiometry (DEXA)

Dual-energy x-ray absorptiometry (DEXA), an imaging modality, is the current standard for evaluating bone quality. DEXA applies a high energy beam and a low energy beam to generate an attenuation profile that has an amplitude proportional to the amount of bone mineral content (BMC). This amplitude is used to calculated the BMC of the bone, while bone mineral density (BMD) or areal BMD is computed by taking the ratio of BMC to projected area (Djokoto, 2002).

$$BMD = \frac{BMC}{\text{Projected Area}} \qquad \textbf{(1.3)}$$

DEXA is currently the standard in noninvasive bone assessment tools since the World Health Organization uses BMD calculated from DEXA to define osteoporosis as a BMD measurement that is 2.5 standard deviations below the mean of a young adult population, whereas osteopenia is one standard deviation below normal (WHO, 1994). Research studies have investigated the clinical capability and reliability of DEXA, concluding that:

- DEXA BMD of the human femur was shown to strongly correlate with bending strength ($R^2$=0.79) and rigidity or stiffness ($R^2$=0.81) (Stromsoe, 1995).
- DEXA BMC of the human radius was shown to have a high correlation with failure moments from 3-pt bending ($R^2$=0.96) (Hudelmaier, 2004).
- DEXA has good precision, low radiation dosage, stable calibration methods, and fast scan times. There are also databases of reference data allowing patient measurements to be compared against thousands of other people of the same gender and/or ethnic origins (Djokoto, 2002).

The disadvantages of DXA include radiation exposure, high medical costs of equipment and clinical scan, large size of the device, and two-dimensional projection measurements. Two-dimensional BMD measurements exclude the thickness of the bone being scanned and can result in false diagnosis of osteoporosis (Carter, 1992). In addition, the minor structural changes in cortical wall thickness that are not detected with

DEXA measurements may significantly affect bone strength (Adami, 1999; Jarvinen, 1999; Khan, 2001). The accuracy of DEXA is also limited by the composition of the soft tissue since the attenuation of the X-ray differs between fat and lean tissue. This difference can produce BMD measurement errors up to 6% (Svendsen, 1995).

### 1.3.2 Quantitative Computed Tomography (QCT)

Quantitative computed tomography (QCT) improves upon the capability of DEXA with the capacity for three-dimensional measurements. . The advantage of QCT is the ability to isolate the area of interest from surrounding tissue; in addition, peripheral quantitative computer tomography (pQCT) is an alternative to QCT that allows for reduced radiation dose by limiting measurement sites to the limbs. Numerous studies have also evaluated the clinical capability and reliability of QCT, concluding that

- QCT has been shown to effectively distinguish between cortical and trabecular bone specimens (Adami, 1999; Jarvinen, 1999) and eliminate soft tissue artifacts (Lochmuller, 2002).
- The precision of QCT is similar to DEXA in distinguishing osteoporotics from normals (Kroger, 1999),
- Measurement of bone mass by pQCT was shown at best to be surrogate measure of bone strength and fracture risk at the distal radius (Hudelmaier, 2004)
- Derived pQCT indices have shown better correlation with failure loads in goat humeri and femurs than BMD from DEXA measurements (Siu, 2003).

The disadvantages of QCT include a much larger radiation dose (30 times larger than DEXA), long scan times (approximately 30 minutes), large machine size, and higher medical costs. Peripheral QCT (pQCT) measurements of BMD at non-specific sites of the skeleton were inferior to spinal DEXA and regular QCT, and for predicting strength in the thoracic spine (Lochmuller, 2002). In addition, pQCT measurements of the weight bearing lower limb do not have an advantage over that of the distal radius (Hudelmaier, 2004), and pQCT provided significantly lower correlations with femur fracture strength than DEXA (Lochmuller, 2003). Furthermore, DEXA and QCT estimate static properties of bone, but give no insight to the characteristics of bone under active or dynamic loading conditions. DEXA and QCT technologies base their measurements for mechanical properties of bone on the intensity of bone mineral content present in the bone. However, vibrational techniques are able to define properties from mechanical waves. Vibrational techniques can estimate not only the stiffness but also the damping of the mineral content of bone, which may accurately characterize the "quality" of bone.

### 1.3.3 Quantitative Ultrasound (QUS)

Applications of ultrasound have been around for over 60 years; however, the medical applications of quantitative ultrasound (QUS) have grown exponentially since ultrasound involves no radiation exposure and is portable, inexpensive, and noninvasive. QUS is a clinical technique that applies high frequency (1-10 MHz) to measure the speed of sound (SOS) through bone. QUS measures the attenuation of the sound signal to estimate BMD and is readily used as a screening tool to identify patients who may require further skeletal evaluation (DEXA or QCT). QUS, however, is hindered by soft tissue attenuation; therefore, only peripheral sites on the limbs and spinous processes can be measured. QUS measurements were shown to have a significantly lower association with bone strength of the spine, femur, or radius in comparison to DEXA and QCT (Lochmuller, 2002). In addition, QUS measurements provided no additional significant trends or evidence in the fracture prediction for the human radius and femur (Hudelmaier, 2004; Lochmuller, 2002).

## 1.4 Mechanical Response Tissue Analysis

Mechanical response tissue analysis (MRTA) was created to examine the stiffness of long bones across a range of frequencies. MRTA is a technology that predicts the average cross-sectional bending stiffness (EI) of long bones based on their response to low frequency, low amplitude vibration. EI is a measure of bone integrity which is directly related to the composition, geometry, and internal architecture of the bone (Steele, 1988). The MRTA technique was initially created by Stanford University researchers in collaboration with NASA to assess bone mineral content of astronauts during long term space missions. The current MRTA, as shown in Figure 1.6, is noninvasive, portable, and inexpensive and utilizes a vertical loading setup for the tibia.

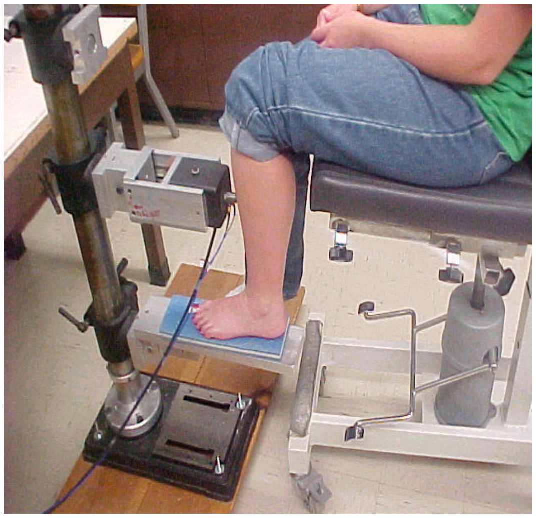

**Figure 1.6: Current MRTA experimental system for tibia strength assessments (reproduced with permission: Herbert, 2004)**

The hardware, shown in Figure 1.6, consists of a mechanical shaker, an impedance head, a contact probe, system controls and measurement software, and analysis software. The shaker, probe, and impedance head, which are connected in series, apply a transcutaneous vibration over the range of 0-1600 Hz for very brief periods (1-2 minutes). The impedance head transmits both force and acceleration data to the measurement software, which converts this real-time data with Fourier transforms into the frequency domain. Upon conversion, the analysis software decomposes the response data into real and imaginary components of stiffness and compliance (inverse of stiffness). The MRTA raw data, shown in Figure 1.7, is a complex stiffness versus frequency response for the tibia at the midshaft. Furthermore, the analysis software curve fits this raw data by applying a specified lumped parameter algorithm.

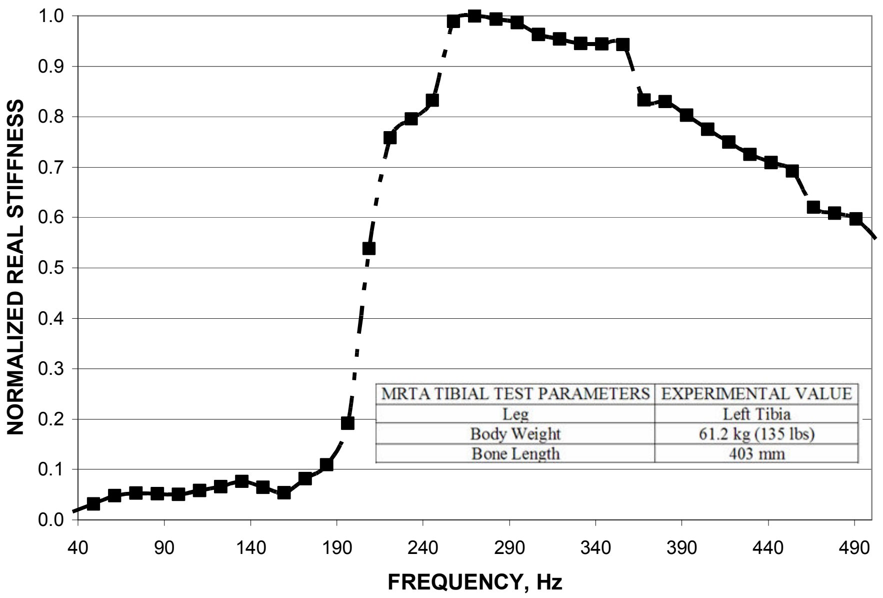

| MRTA TIBIAL TEST PARAMETERS | EXPERIMENTAL VALUE |
|---|---|
| Leg | Left Tibia |
| Body Weight | 61.2 kg (135 lbs) |
| Bone Length | 403 mm |

**Figure 1.7: MRTA experimental stiffness response for human tibia *in vivo***

## 1.5 Summary

In review, there is supporting and contradictory evidence for DEXA, QCT, and QUS in accurately monitoring bone strength. MRTA offers an evaluation of the dynamic mechanical properties of bone *in vivo*. Previous studies have shown strong correlations for the MRTA EI values with BMC, fracture loads, and BMD values. A thorough review of previous MRTA research, provided in the next chapter, further explains the experimental and computational advantages and disadvantages of the device. This review spawned the proposed problem statement and research hypothesis for this thesis, and ultimately to the first FE simulation of the MRTA test of a human tibia.

# 2. Mechanical Response Tissue Analysis (MRTA)

## *2.1 Review*

The current imaging modalities (DEXA, QCT) attempt to quantify bone mineral content and distribution in bone; however, the strength of bone is determined by not just the mineral content and distribution but also the orientation and stiffness of the microstructure. Low frequency vibration techniques, which bypass the quantification of mineral distribution and total mass, evaluate the structural integrity of bone by measuring the stiffness of the material, which is a good indicator of fracture strength (Steele, 1988).

The earliest vibration method attempted to predict bone strength on the basis of the resonant frequencies (Jurist, 1970a and 1970b). The resonant frequency approach was able to find significant differences between osteoporotic women residing in a nursing home and normal age matched women, but was unable to reproduce this result in an outpatient population. Based on this inadequacy, it was concluded that geometric or other systematic differences resulted in a resonant frequency bias that is not truly predictive of osteoporosis. Resonant frequency is the ratio of stiffness to mass which is problematic for detecting osteoporosis because both stiffness and mass decrease (Steele, 1988). The resonant frequency technique was quickly proven insufficient, and paved the way for new, methods that evaluated material properties across a range or "sweep" of frequencies.

Young and colleagues (Young, 1976) were the first to digress from the resonant frequency approach and examine the response of bone to an applied frequency sweep. Their approach estimated the cross sectional bending stiffness (EI) of monkey ulnae and tibiae from an experimental frequency response. Their results showed significant correlation ($R^2$=0.90) between EI and bone mineral content. However, the true potential of low frequency vibration was not clinically relevant until this method was shown to detect adaptations in bone that are not quantified by BMC changes. During six months of semi-reclined constraints, BMC losses in monkey tibiae of 23-31% were measured, while EI decreased from 36-40%. Following the restraints, EI returned to normal after 8.5 months of recovery, but even after 15 months of recovery, BMC did not return to baseline levels (Young, 1983).

In 1988, Steele and colleagues created the mechanical response tissue analyzer (MRTA) from the apparatus and methods used by Young *et al*. (1976; 1983). This pervious version of the MRTA was very similar to the current MRTA (refer to Section 1.4) except their experimental setup utilized a horizontal stand for simply-supported ulnar measurements. Steele (1988) developed a 7-parameter lumped model of the ulna based on beam theory to serve as a computational algorithm to curve fit the real and imaginary stiffness responses of the ulna. The 7-parameter model, shown in Figure 2.1, is a mechanical analog representation of the upper limb that includes: masses for the soft tissue and bone ($m_s \; and \; m_b$), damping for bone and skin ($b_s \; and \; b_b$), stiffness for bone and skin ($k_s \; and \; k_b$), and damping behavior of the skin with respect to the motion of bone ($b_p$).

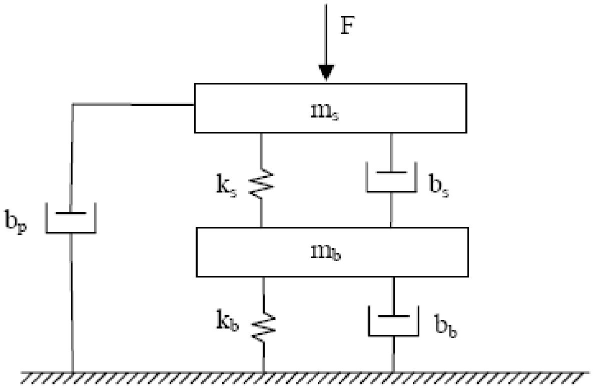

**Figure 2.1: 7-parameter model with masses for the soft tissue and bone ($m_s$ and $m_b$), damping for bone and skin ($b_s$ and $b_b$), stiffness for bone and skin ($k_s$ and $k_b$), and damping behavior of the skin with respect to the motion of bone ($b_p$) (reproduced with permission: Steele, 1988)**

A unique, closed form solution to the 7-parameter model fitted a curve to the MRTA raw data to estimate ulnar EI values. The 7-parameter MRTA algorithm was applied to several experimental studies, which concluded that:

- Ulnar EI measurements showed high correlation ($R^2$=0.81) to bone mineral content with coefficients of variation on the order of 3-5% (Steele, 1988).
- Ulnar EI values correlated with BMC ($R^2$=0.59-0.72) and bone width ($R^2$=0.35-0.67) to accurately detect decreases with age in the ulnae of women (McCabe, 1991).
- The reliability of EI measurements with repositioning was good for the ulna (<5%) but poor for the tibia (5-12%); however, there was correlation between EI values and BMC for the ulna and tibia suggesting that MRTA can detect the functional capacity of bone to adapt to activity (Arnaud, 1991).

- The MRTA technology differentiated between ulnar EI values of stronger, more athletic subjects and age matched subjects of lower habitual exercise levels (Myburgh, 1993).
- Osteoporotic women displayed ulnar EI values 25% lower than the mean value for normal women and 17% lower than osteopenic women. However, no significant difference in EI was found between the osteopenic and normal women (Kiebzak, 1999).

Alternate algorithms based on beam theory were developed to enhance the reliability of EI measurements for the MRTA. Roberts and colleagues (1996) created a 6-parameter mechanical analog, shown in Figure 2.2, for more flexible monkey tibia to incorporate clamped end conditions. This 6-parameter model does not have a closed form algebraic solution; therefore, an iterative process was developed to make an initial approximation of the raw data and then step through refinements that attempt to accurately model the raw data. The 6-parameter model for long bone vibration in clamped end conditions was validated through the experimental testing of aluminum rods with padding to simulate skin. The relationship between MRTA EI measurements and theoretical stiffness values of the rods was $R^2=0.999$. The 6-parameter model was further validated through testing of flexible, excised monkey tibiae and compared to three-point bending results of the same tibiae. The correlation between stiffness from three-point bending and MRTA bending stiffness values was very strong ($R^2=0.95$), which was stronger than previous results using the 7-parameter model for the tibia (Roberts, 1996).

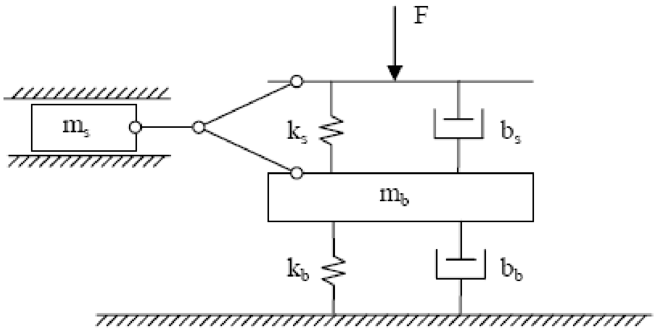

**Figure 2.2: 6-parameter model with masses for the soft tissue and bone ($m_s$ and $m_b$), damping for bone and skin ($b_s$ and $b_b$), and stiffness for bone and skin ($k_s$ and $k_b$) (reproduced with permission: Steele, 1996)**

Subsequent research on the MRTA has introduced newer, more advanced computational algorithms to accurately estimate the vibrational response of the tibia. The MRTA 6- and 7-parameter models have produced significant and reliable results for the human ulna due to its fairly uniform structure (i.e. resembles a long cylindrical tube). These models, however, have shown inconclusive EI measurements for the tibia due to its complex geometry and material composition. Therefore, 9- and 12-lumped parameter models were developed in conjunction with the MRTA hardware to evaluate the mechanical integrity of the tibia. The 9-paramter model is similar to a cantilever beam representation in that the proximal tibia is pinned and the distal tibia is free to vibrate. The 12-parameter model, shown in Figure 2.3, allows for both the proximal and distal ends (knee and ankle joints) of the tibia to vibrate freely. The goal of the 12-parameter model was to eliminate supporting hardware for the lower limb and reduce error introduced by the technician's level of training (Callaghan, 2003).

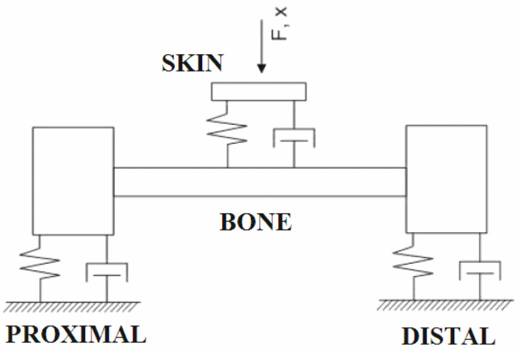

**Figure 2.3: 12-parameter model for the human tibia (reproduced with permission: Steele, 2006)**

Previous repeatability studies reviewed the performance of the 6-, 7-, 9-, and 12-lumped parameter models for the MRTA. These studies all investigated the current MRTA device (refer to Figure 1.7) to examine the repeatability of EI measurements for the human tibia. Thorne (2000) evaluated the 7-parameter model for inter- and intra-reliability of tibial EI measurements for 22 healthy college women. Poor between-trial reliability with high coefficients of variation (on the order of 30%) was reported after tibial EI assessments were performed twice per day for three consecutive days. Miller (2002) evaluated the 6-, 7-, 9-, and 12-parameter MRTA models for tibial EI reliability in 12 college-aged women. Composite tibiae or Sawbones (Pacific Research Laboratories, Inc, Vashon, Washington), which are mechanical analogs of the tibia that match stiffness and geometry, were also evaluated with these models and compared to three-point bending tests of the Sawbones©. The between-trial coefficient of variation was 15% (12-parameter) for tibial EI measurements while the within-trial and between-day coefficients (7-parameter) of variation were 20% and 19%, respectively. There was no relationship or correlation between the three-point bending values and MRTA EI measurements for the Sawbones© due to the large discrepancies associated with the EI values from the MRTA (Miller, 2002).

The first study devoted to the 12-parameter MRTA model investigated the reliability of tibial EI measurements in a much larger subject pool of 110 college-aged females (Callaghan, 2003). The current MRTA system demonstrated an improvement in within-trial reliability for unsupported tibial EI measurements with a coefficient of variation of 11.2%. These results demonstrated the ability of the system to measure tibial response characteristics when both proximal and distal ends are free of rigid support. Long-term measurement reliability was still problematic with a coefficient of variation of 36.5% for a set of 4 measurements spanning 21 months (Callaghan, 2003).

In more recent studies, the MRTA was further evaluated and compared to measurements from dual-energy x-ray absorptiometry (DEXA) and quantitative ultrasound (QUS). Ulnar EI was measured using the MRTA for 56 healthy volunteers (20 men and 36 women) and compared to measurements of speed of sound (SOS) from QUS and BMC and BMD measured from DXA. The MRTA EI values correlated with the DEXA measurements especially at the midshaft of the ulna, but no significant correlation was found between MRTA and QUS measurements.

World class athletes of different loading regimes were also investigated using the MRTA to determine its effectiveness in prediction long bone strength (Liang, 2005). The tibiae and ulnas of 13 synchronized swimmers, 8 gymnasts, and 16 untrained women were examined using the 12-parameter MRTA model to evaluate the differences in EI among these groups. The MRTA device in this study applied a direct vibration to the midshaft of the tibia and ulna with a horizontal probe position. In addition, repeatability of the device was experimentally tested on the same individual using the 7-, 9-, and 12-parameter algorithms. Based on the 7-parameter algorithm the coefficient of variation

(CV) of ulnar EI was 3.2% and on the 9-parameter algorithm 5.6%. Based on the 12-parameter algorithm, the CV of tibial EI was 10.8%. For the group comparison, ulnar EI was similar in the synchronized swimmers and gymnasts and 50% higher than in the untrained groups. Tibial EI was slightly larger in gymnasts than swimmers and more than twice as high in the untrained women (Liang, 2005).

## 2.2 Problem Statement

The MRTA is a noninvasive, strength assessment technology that estimates the EI of long bones at the midshaft through low frequency, low amplitude vibration. The MRTA hardware computes the complex stiffness response (in the frequency domain) of the long bone while the MRTA software attempts to match a prediction curve to the experimental raw data to estimate EI. Previous MRTA research has used several prediction models (6-, 7-, 9-, and 12-parameter) to interpret the response of the human tibia during vibration, but estimated EI measurements are still not adequate to warrant clinical value for the MRTA. These prediction algorithms assume linear stiffness and damping constants for bone tissue, skin tissue, and proximal and distal constraints. However, the overall dynamic damping response of bone may not be correctly assumed by a single damping parameter. Therefore, these lumped parameter components may incorrectly represent their anatomical counterparts, and this inaccuracy may be a direct cause of the inadequate reliability associated the MRTA tibial strength assessments.

The experimental raw data or complex stiffness versus frequency response measured by the MRTA offers a wealth of information on the bone material and structural composition. For example, MRTA EI measurements for the ulna and the tibia in the frequency domain were verified with significant correlations to BMC and experimental stiffness values from three-point bending tests. This suggests that the experimental stiffness response of the MRTA is effectively quantifying the mechanical stiffness of the bone material *in vivo*. However, alternate parameters in the frequency domain, such as bone damping, may also accurately characterize bone integrity for long bones in vibration. Therefore, identifying dominant parameters in the frequency response would be useful to make linear prediction models more suitable for estimating the bone integrity under low frequency, low amplitude vibration.

Therefore, it is practical to systematically determine through finite element analysis (FEA) which parameters dominate the complex stiffness response during a MRTA test of a human tibia. FEA provides a unique engineering tool to control material and structural aspects in order to detect dominant parameters in the frequency domain during simulated vibration. Material behavior, geometry, internal architecture, and boundary conditions for the tibia can be manipulated to verify alternate parameters in the linear prediction models and possibly single out specific limitations associated with a particular lumped parameter component. Verification of dominant parameters in the frequency domain would improved prediction of the complex stiffness response for the tibia and may provide further insight into the software and hardware limitations that have plagued reliability in MRTA strength assessments.

## 2.3 Hypothesis

This thesis presents the first finite element (FE) simulation of the MRTA test of a human tibia. This FE simulation incorporates a unique, FE procedure, known as direct steady state dynamics (DSSD), to calculate the complex stiffness versus frequency response of the human tibia. DSSD applies a harmonically oscillating force to the midshaft of the tibia over a range of frequencies to simulate the MRTA strength test. Natural frequency analysis, static analysis, and DSSD procedures in ABAQUS (v6.5) were applied to a series of finite element parametric studies to evaluate different material behaviors, geometries, and knee and ankle constraints for the tibia. The research hypothesis states that these parametric studies for different material behaviors, geometries, and boundary conditions can identify dominant parameters in the frequency response.

The specific aims in this thesis are:

1) The DSSD procedure will be validated by the analytical solution of a prismatic and hollow-cylindrical beam in vibration.
2) Increasing complexity (complex geometry and material behavior) of tibia models will more accurately reproduce previous experimental and computational bending modes for an actual human tibia.
3) Increasing complexity including viscoelastic material behavior and complex tibial geometry will better simulate the experimental dynamic response of the tibia from MRTA strength tests.
4) The DSSD procedure will expose a unique set of boundary conditions at the proximal and distal regions of the tibia that produces a response curve most similar to the MRTA experimental raw data.
5) Inclusion of soft tissue effects into the FE simulation will further match the experimental raw data from the MRTA tibia test.

# 3. Models and Methods

Finite element analysis (FEA) is a very useful engineering tool in orthopedic and biomedical applications due to the complex, irregular geometries and material properties associated with anatomic structures and their functions. Due to irregular geometry and composition of the tibia, FEA was considered an ideal application to simulate the MRTA vibrational technique. In this thesis, the first FEA simulations for the MRTA test of a human tibia were created, tested, and validated. To simulate the MRTA, the commercial FE software, ABAQUS (v6.5), was employed to investigate the bone response to static and dynamic loading and test the research hypothesis. ABAQUS, more specifically ABAQUS/Standard, was used due to its remarkable abilities to efficiently analyze large, complex meshes (such as the whole tibia) as well as frequency-dependent material properties that govern bone and soft tissue.

## *3.1 FE Models*

Finite element models for the human tibia were created from the *CT_Fronzen_TIBIA_DX_RI* solid model downloaded from the BEL repository (Viceconti, 2003). The *CT_Fronzen_TIBIA_DX_RI* solid model contains the external surface geometry of the human tibia, which was derived from the Visible Human Project (VHP). The software, PATRAN (v2005), was used as a solid modeling interface to create a combination of tetrahedral and hexagonal elements that were used to mesh the geometric aspects of the human tibia. Five models of increasing complexity were developed in stages to examine the different effects that material properties, geometry, and knee and ankle constraints had on the dynamic response of the tibia. The length of the FE tibia equaled 406.4 mm, and each model subsequently increased in complexity from the previous representation. The five models investigated were the Solid Model, the Hollow Model, the Bi-Material Model, the Viscoelastic Model, and the Skin Model. Each model had properties of its predecessor and was named for the added complexity. For example, the medullary canal was added to the Solid Model to create the Hollow Model and a viscoelastic skin layer was added to the Viscoelastic Model to generate the Skin Model.

### 3.1.1 The Solid Model

The Solid Model was the first computational model created for simulation of the MRTA technique. The Solid Model had 20,268 tetrahedral elements and 4,341 nodes to represent the diaphysis and epiphyses of the tibia, as shown in Figure 3.1. The Solid Model was completely homogenous and solid with each element considered to be cortical bone, isotropic, and linear-elastic (LE) in material behavior. The material properties for cortical bone, shown in Table 3.1, were taken from the literature and implemented into the Solid Model (An, 2000).

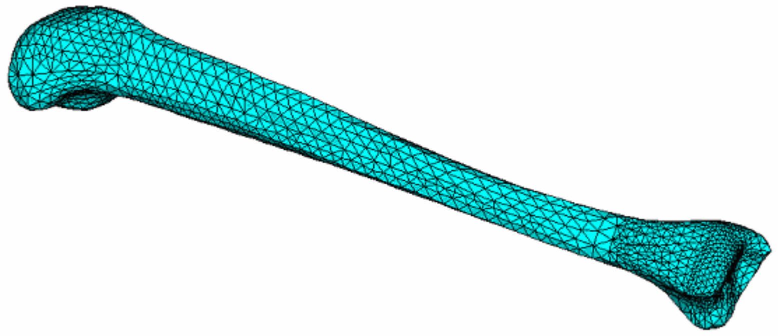

**Figure 3.1: The solid model**

**Table 3.1: Material properties for human cortical bone**

| Material Property | Published Value (An, 2000) |
|---|---|
| Young's Modulus, E | 17 GPa |
| Poisson's Ration, v | 0.33 |
| Density | 1.85 g/cm$^3$ |

### 3.1.2 The Hollow Model

The Hollow Model, shown in Figure 3.2, was developed to provide a better anatomical representation of the human tibia. The geometry of the medullary canal was added to the Solid Model using the tibial cross sectional shown in Figure 3.3a. This cross section was extruded through the length of the diaphysis to create the medullary canal of the FE model for the tibia. The medullary canal, shown in Figure 3.3b, was hollow, and the cortical shell was meshed with 2,760 hexagonal elements. The distal and proximal epiphyses were meshed with 8,228 tetrahedral elements. The nodes between the hexagonal (diaphysis) and tetrahedral (epiphyses) elements were connected as shown in Figure 3.3c. In total, the Hollow Model contained 5,509 nodes and 10,988 elements. The Hollow Model was also isotropic and homogenous consisting of entirely cortical bone using the same material properties as the Solid Model (see Table 3.1).

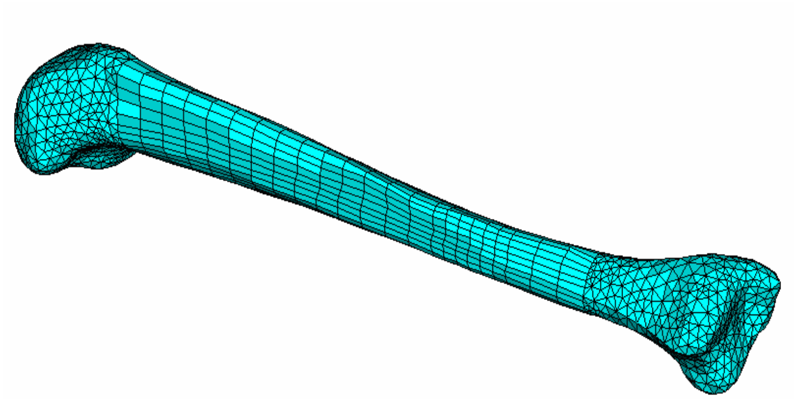

**Figure 3.2: The hollow model**

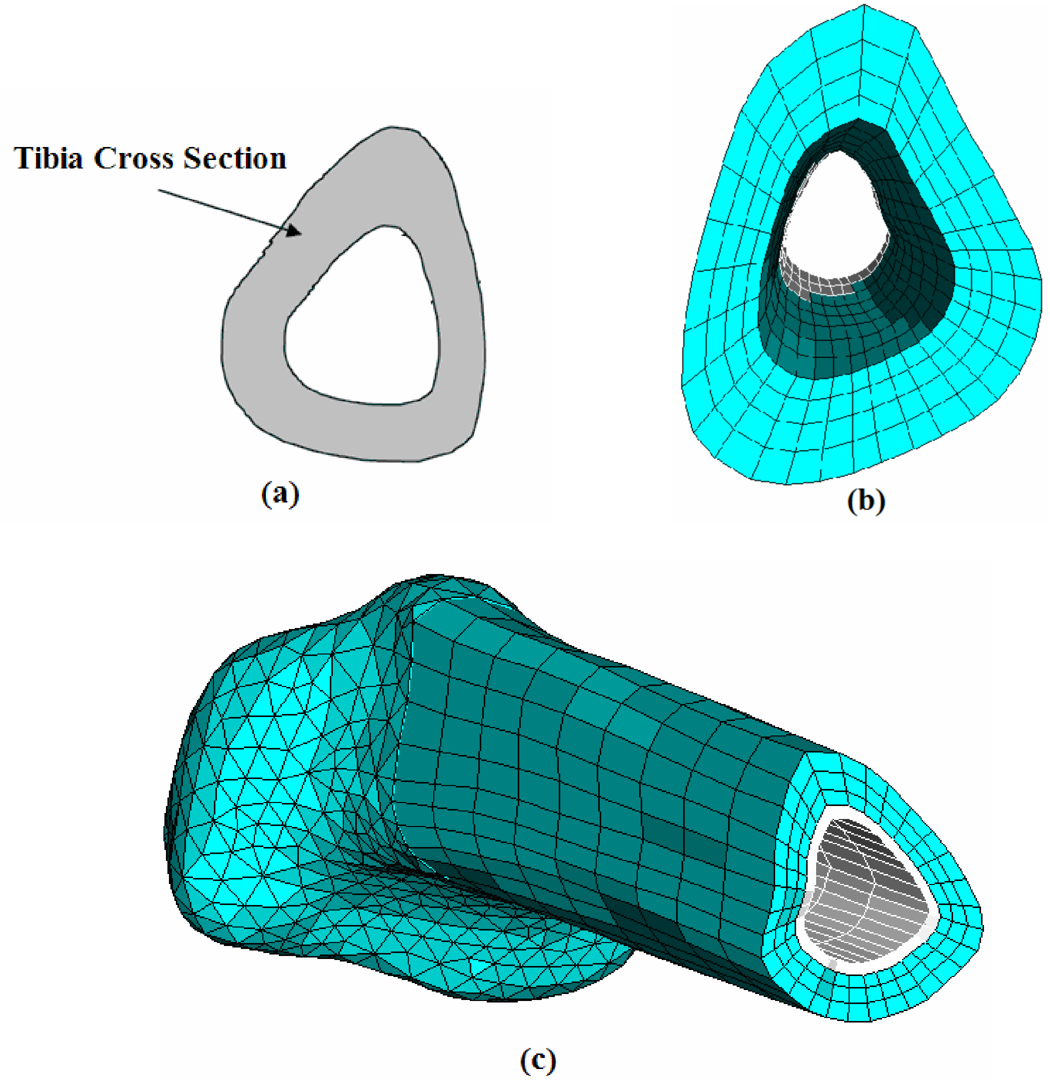

**Figure 3.3: (a) Actual tibia cross section (reproduced with permission: Callaghan, 2003) (b) FE tibia cross section with only hexagonal elements (c) proximal end with tetrahedral elements connected to hexagonal elements**

### 3.1.3 The Bi-Material Model

Cancellous or trabecular bone properties were added to the epiphyses of the Hollow Model to create the Bi-Material Model. Cancellous bone was added to further simulate the non-homogenous composition of the human tibia and included the softer cancellous bone at the proximal and distal ends of the human tibia. Cancellous ends, as shown in Figure 3.4, were introduced to better simulate the vibrational response of the tibia under the simulated MRTA experimental conditions. Cancellous elements were assigned with isotropic and linear elastic values from previously reported material properties, shown in Table 3.2.

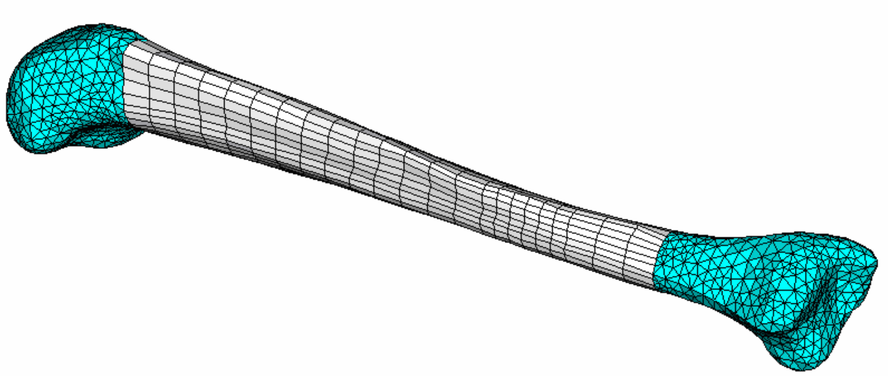

**Figure 3.4: The bi-material model: white and blue elements are cortical and cancellous bone, respectively**

**Table 3.2: FE material properties for cancellous and cortical bone**

| **Material Property** | **Published Value (An, 2000)** |
|---|---|
| Cortical Bone: | |
| E | 17 GPa |
| v | 0.33 |
| density | 1.85 g/cm$^3$ |
| Cancellous Bone: | |
| E | 445 MPa |
| v | 0.33 |
| density | 0.29 g/cm$^3$ |

### 3.1.4 The Viscoelastic Model

Linear elastic material behavior was replaced with frequency dependent viscoelastic properties to create the Viscoelastic Model. Linear viscoelasticity has been shown to represent the material behavior of bone through complex, frequency-dependent experimentation (Lakes, 1982; Garner, 2000). Since the MRTA applies a frequency sweep to the tibia, the frequency dependent material properties likely play a significant role in the vibrational response of the bone. Therefore, experimental values for the storage and loss moduli of cortical and cancellous bone were taken from the literature and inputted into the Viscoelastic Model (Lakes, 1982; Garner, 2000; Dong, 2004). Appendix A provides a brief explanation of linear viscoelasticity, lists the experimental values, and shows the mathematically calculations used to solve for the frequency dependent input variables associated with ABAQUS.

### 3.1.5 The Skin Model

Finally, a skin layer under the forcing probe was added to the tibial crest at the midshaft to create the Skin Model. This skin layer was the final complexity evaluated in the simulation of the MRTA technique. The skin layer was created to simulate the minimal soft tissue that exists between the tibia surface and probe during the MRTA experimental testing. At the tibial crest, 6 linear hexagonal elements that were 2mm thick were added. This thickness was chosen to simulate the minimal tissue layer between the probe and tibia due to the preload of the mechanical shaker. The skin elements were assigned frequency-dependent viscoelastic values (see Appendix A).

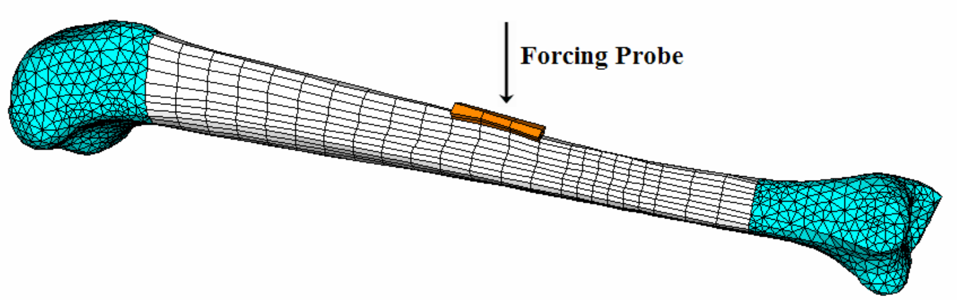

Figure 3.5: The skin model

### 3.1.6 Boundary Conditions

Each of the above FE models was experimentally analyzed with four different boundary conditions (BC) to evaluate the effect of constraints on the complex stiffness response of the tibia under vibration. The current interpretation of the MRTA utilizes a 12-parameter "free-free" end condition model for the tibia. However, previous MRTA algorithms have used "pinned-free" and "pinned-pinned" boundary constraints to experimentally fit the MRTA raw data. To better interpret the relationship between experimental MRTA and distributed parameter FE response, boundary conditions were applied to a set of nodes at the proximal and distal regions of each FE model in relation to a (*x,y,z*) coordinate system, as shown in Figure 3.6. The boundary conditions reflect anatomical constraints on the translational motion at the proximal and distal tibia. Rotational effects on the tibia during vibration were not considered. Table 3.4 defines the four boundary conditions used to evaluate the complex stiffness versus frequency response for the tibia in vibration.

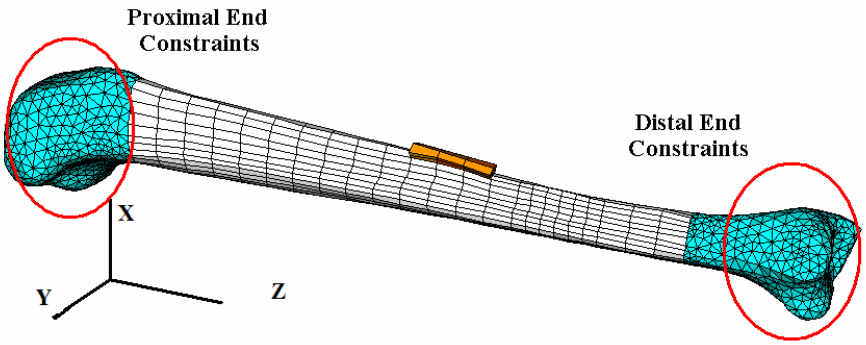

**Figure 3.6: Boundary condition regions for proximal and distal ends of tibia**

**Table 3.3: FE boundary conditions (✓=no translation)**

| FE Constraints | Proximal | | | Distal | | |
|---|---|---|---|---|---|---|
| | *x* | *y* | *z* | *x* | *y* | *z* |
| Clamped-*xy* | ✓ | ✓ | ✓ | | | ✓ |
| Clamped-*z* | ✓ | ✓ | ✓ | ✓ | ✓ | |
| Clamped-free | ✓ | ✓ | ✓ | | | |
| Free-free | | | | | | |

## 3.2 FE Analyses

### 3.2.1 Static Analysis

The static analysis simulated the preload of the MRTA on the tibia. The preload from the weight of the mechanical shaker has been reported to range from 8-10 N (Roberts, 1996; Steele, 1988). In addition, this preload has been shown to sufficiently minimize the nonlinear soft tissue effects in the vibrational response of the tibia and more effectively estimate EI of the bone itself (Roberts, 1996). Therefore, a static preload of 10 N was used in each analysis and was chosen as a concentrated force applied at the tibial crest midshaft, as shown in Figure 3.7.

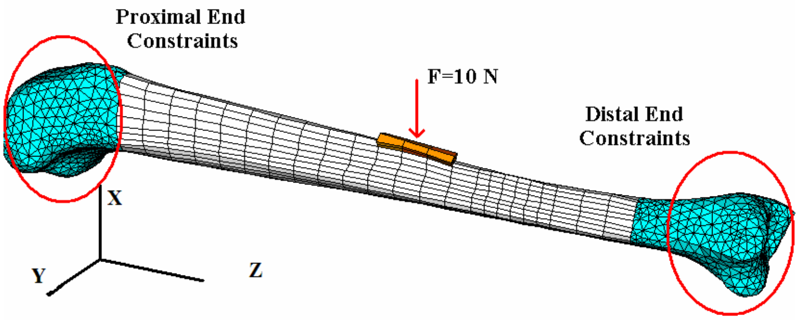

**Figure 3.7: Static loading of tibia**

### 3.2.2 Natural Frequency Analysis

Natural frequency analysis (ABAQUS) is an eigenvalue extraction procedure that determines the mode shapes and natural frequencies of a structure. The natural frequency analysis was used to verify that the FE models were structurally accurate in representing an actual human tibia. The bending modes of the four FE tibia models (excluding the Skin Model) were analyzed and compared to previous experimental and computational results to verify these models.

### 3.2.3 Direct Steady-State Dynamics Analysis (DSSD)

The direct steady-state dynamics (DSSD) procedure in ABAQUS was used to determine the complex stiffness versus frequency response of the tibia, This procedure was used to calculate the steady-state dynamic linearized response of the FE model to harmonically forced excitation. The DSSD analysis calculates the response of the system in terms of the physical degrees of freedom of the model due to a harmonically oscillating excitation during a frequency sweep. The equations of motion for these degrees of freedom are solved at each specified frequency within the sweep. Using the DSSD procedure, a 0.4 N amplitude vibration was applied to calculate the displacement response at the midshaft of the tibia over the range of 40-500 Hz, which was chosen to emulate the experimental frequency sweep of the MRTA. The force to displacement ratio or stiffness response was calculated for all boundary conditions for each model in the specified frequency range.

### 3.2.4 FE Procedure Validation

The FE analysis technique was validated before any FE tibia models were investigated. This validation was necessary to ensure that the applied FE procedures accurately calculated the static and dynamic response of a structure. The FE validation evaluated two, three-dimensional FE models: a prismatic beam and a hollow cylindrical beam. The computational results were compared to analytical solutions for a prismatic and hollow cylindrical beam, which are located in Appendix B. The results of this comparison are located in Appendix C, and they showed excellent agreement between the analytical solution and all three FE analyses for both the prismatic and hollow-cylindrical beams. This validation demonstrates that the FE analyses performed in this thesis were valid in determining the accurate static and dynamic response of a structure, which allowed for dependable analysis of the FE tibia models.

## *3.3 FE Parametric Studies*

Table 3.4 provides a detailed description of each parametric run performed in this thesis. The parametric studies were analyzed using ABAQUS to evaluate different material properties, geometries, and constraints. The goal of these studies was to identify dominant parameters in the frequency response that would be useful to make linear prediction models more suitable for estimating the bone integrity under low frequency, low amplitude vibration. Table 3.4 refers to several figures that are located in Appendix D; however, conclusions and significant trends are reported in the following chapter.

## Table 3.4: Parametric studies

| PARAMETRIC STUDIES: | MODEL(S) EVALUATED | METHODS/BC's | RESULTS |
|---|---|---|---|
| 1. **Boundary Conditions**<br>a. Applied nodal constraints to proximal and distal nodes | All Models | Refer to Table 3.3 | Figure 4.4 |
| 2. **% of Constrained Nodes**<br>a. Number of nodes being constrained was evaluated<br>b. Used Pinned-*xy* BC | Viscoelastic Model (cortical only) | Constrained percentage of nodes at proximal and distal tibia | Figure 4.6 |
| 3. **Location of Constrained Nodes**<br>a. Nodes at bottom of proximal and distal tibia were constrained<br>b. Used Default BC** | Viscoelastic Model (cortical only) | Constrained nodes at bottom/posterior surface of proximal and distal tibia | Figure 4.8 |
| 4. **Cancellous Viscoelasticity**<br>a. Added linear viscoelasticity behavior to cancellous bone<br>b. Used Default BC | Viscoelastic Model (both cortical and cancellous bone) | f, E', E'', G', G'' taken from literature and inputted into FE simulation for cancellous bone (Dong, 2003) | Figure D.1 |
| 5. **Skin Layer/Soft Tissue**<br>a. Added soft tissue properties at tibia surface to act as skin layer between forcing probe & tibia<br>b. Evaluate skin layer effects on dynamic response<br>c. Used Default BC | Skin Model (cortical, cancellous, & soft tissue) | f, E', E'', G', G'' taken from literature and inputted into FE simulation for soft tissue. Properties derived from experimental tests on material similar to human ligament tissue) (Ambrosio, 1998) | Figure D.2 |
| 6. **Soft Tissue @ Ends**<br>a. Added soft tissue properties to proximal & distal ends<br>b. Applied BC to soft tissue nodes<br>c. Used Default BC | Skin Model (cortical, cancellous, & soft tissue) | Same as Parametric Study #5, but soft tissue elements were added to proximal and distal ends | Figure D.3 |
| 7. **Revised Skin Properties**<br>a. Changed skin properties to better simulate MRTA experimental *in vivo* response for tibia & soft tissue<br>b. Soft Tissue @ ends was ignored.<br>c. Used Default BC | Revised Skin Model (includes viscoelastic properties from actual dynamic experiments for rabbit skin) | f, E', E'', G', G'' taken from literature and inputted into FE simulation for skin (Pereira, 1991) | Figure 4.10 |
| 7. **Skin Thickness**<br>a. Evaluate effects of different thicknesses for skin layer<br>b. Soft Tissue @ ends was ignored.<br>c. Used Default BC | Skin Model (previous skin properties for soft tissue based on ligamentous material) | Evaluated 0.5, 2, & 4mm thickness for skin layer | Figure 4.11 |
| 8. **Spring/Dashpot Constraints**<br>a. Replaced constrained nodes with linear 1-DOF springs & dashpots<br>b. No boundary condition | Revised Skin Model | Spring Constant=1000 N/m<br>Damping Constant=100 N-sec/m | Figure 4.12 |
| 8. **Cortical Bone Evaluation**<br>a. Evaluated effects of weaker & stronger cortical bone<br>b. Compared 30% reduction & 30% increase in stiffness<br>c. Used Default BC<br>d. Used Spring/Dashpot Constraints | Viscoelastic Model (cortical & cancellous) | 30% increase<br>30% decrease<br>in Cortical Bone E' & E'' | Figure 4.13<br>Figure 4.14 |

**NOTE: Default BC refers to the Pinned (proximal)-*xy* (distal) boundary condition. This BC was considered the most ideal for the MRTA simulation. This Default BC included 67% of proximal nodes constrained and 56% of distal nodes constrained.

# 4. Results

## 4.1 Model Verification

The validation of the static, natural frequency, and DSSD procedures showed that each FE analysis accurately determined the static, structural, and dynamic response of different geometric beams (see Appendix C). The natural frequency analysis was further used to calculate the bending modes and resonances for the FE tibia models. The bending modes of the FE tibia models were then compared to previous experimental and computational data for human tibiae. This bending mode comparison was necessary to verify that the proposed FE tibia models accurately represented the structural response of a human tibia during vibration.

Each model was evaluated with the natural frequency analysis (ABAQUS) to investigate the structural and geometric accuracy of the FE tibia models under different knee (proximal tibia) and ankle (distal tibia) constraints (see Section 3.1.6). Constraints, shown in Figure 4.1, were applied to 67% of surface nodes at the proximal tibia and 56% of surface nodes at the distal tibia.

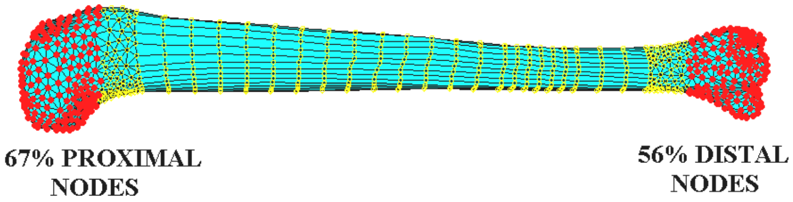

**Figure 4.1: Applied nodal constraints at proximal and distal tibia**

Bending modes of the FE models were observed in the medial-lateral plane and the sagittal or frontal plane, which was expected due to the previous validation results for the prismatic and hollow-cylindrical beams (see Appendix C). For free-free boundary conditions, Figure 4.2 depicts the first and second bending modes in the medial-lateral bending plane while Figure 4.3 shows the first bending mode in the sagittal plane for the Viscoelastic Model.

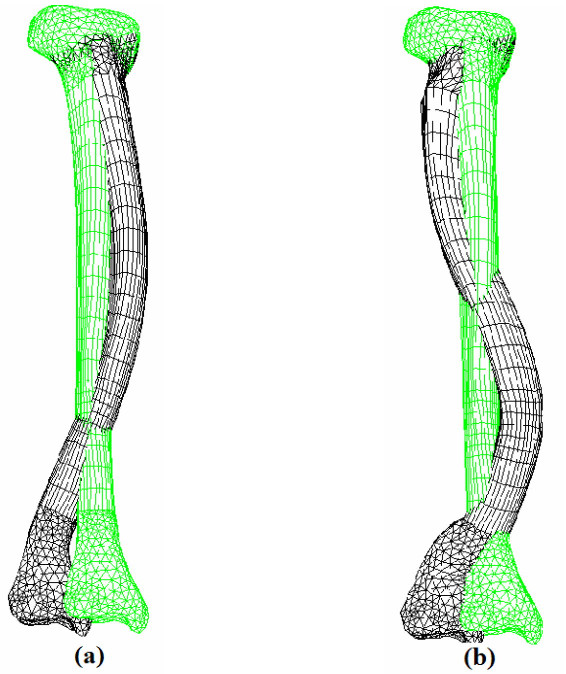

**Figure 4.2: Medial-lateral bending modes plotted against the undeformed tibia for the viscoelastic model (a) 1st mode (b) 2nd mode**

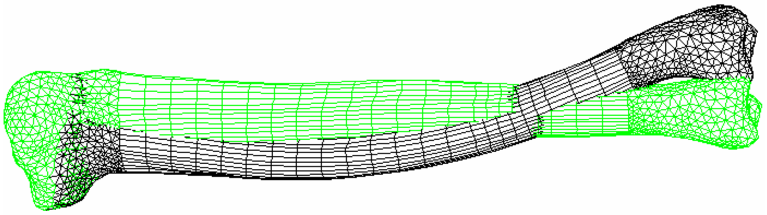

**Figure 4.3: 1st sagittal bending mode for viscoelastic model plotted against the undeformed tibia**

Qualitatively, the modal shapes for the FE models were similar to previous finite element studies of the human tibia (refer to figures in Lowet, 1996 and Hobatho, 1991).

In addition, previous experimental *in vivo* and *in vitro* bending modes for the human tibia were reviewed and compared to each FE model. These values are listed in Tables 4.1, 4.2, and 4.3.

**Table 4.1: Bending modes and boundary conditions for FE tibia models**

| **FE MODELS & BOUNDARY CONDITION RESULTS** | | **Clamped-*xy*** | | **Clamped-*z*** | | **Clamped-free** | | **Free-free** | |
|---|---|---|---|---|---|---|---|---|---|
| | | M-L | Sagt. | M-L | Sagt. | M-L | Sagt. | M-L | Sagt. |
| SOLID | *Mode 1 (Hz)* | 786 | 953 | 805 | 974 | 96.7 | 127 | 320 | 403 |
| | *Mode 2 (Hz)* | 2210 | 2317 | 2004 | 2369 | 550 | 694 | 1007 | 1280 |
| | | | | | | | | | |
| HOLLOW | *Mode 1* | 873 | 1067 | 891 | 1089 | 93.1 | 124 | 324 | 416 |
| | *Mode 2* | 1868 | 2511 | 2146 | 2565 | 576 | 737 | 1061 | 1328 |
| | | | | | | | | | |
| BI-MATERIAL | *Mode 1* | 392 | 483 | 404 | 498 | 90.3 | 125 | 455 | 550 |
| | *Mode 2* | 1139 | 1273 | 1179 | 1298 | 449 | 548 | 885 | 1060 |
| | | | | | | | | | |
| VISCOELASTIC | *Mode 1* | 396 | 492 | 408 | 507 | 90.7 | 125 | 455 | 550 |
| | *Mode 2* | 1158 | 1291 | 1200 | 1310 | 448 | 547 | 885 | 1060 |

**Table 4.2: Bending modes and boundary conditions for previous FEA studies**

| **FEA STUDY & BC RESULTS** | | **Clamped-*xy*** | | **Clamped-*z*** | | **Clamped-free** | | **Free-free** | |
|---|---|---|---|---|---|---|---|---|---|
| | | M-L | Sagt. | M-L | Sagt. | M-L | Sagt. | M-L | Sagt. |
| HIGHT~1980 | *Mode 1 (Hz)* | 168 | 226 | 282 | 226 | 91.7 | 131 | 298 | 420 |
| | *Mode 2 (Hz)* | 720 | 938 | 768 | 960 | 465 | 610 | 938 | 1205 |
| | | | | | | | | | |
| HOBATHO~1991 | *Mode 1* | | | | | | | 504 | 416 |
| | *Mode 2* | | | | | | | 1140 | 1260 |
| | | | | | | | | | |
| LOWET~1996 | *Mode 1* | | | | | | | 403 | 519 |
| | *Mode 2* | | | | | | | 1168 | 1376 |

**Table 4.3: Previous *in vivo* and *in vitro* bending modes for human tibia**

| **TIBIA RESONANCES & BC RESULTS** | | | | **Clamped-*z*** | | | | **Free-free** | |
|---|---|---|---|---|---|---|---|---|---|
| | | | | M-L | Sagt. | | | M-L | Sagt. |
| Van Der Perre~1983 | *Dry, excised tibia* | | | | | | *Nat. Freq. Range* (Hz) | 424-690 | 659-926 |
| | *Fresh, excised tibia* | | | | | | *Nat. Freq. Range* (Hz) | 310-392 | 412-421 |
| | *Dry, excised with injected grease (as bone marrow)* | | | | | | *Nat. Freq.*(Hz) | 357 | 465 |
| | | | | | | | | | |
| Christensen ~1986 | *Wet, excised tibia* | Pinned-pinned | | 337 Hz | | | | 476 Hz | |
| | *Hanging Leg (In Vivo)* | | | | | | | 470 Hz | |

*Empty spaces represent no data or results that were not reported.
*M-L=Medial-Lateral Plane
*Sagt.=Sagittal Plane

In Tables 4.1, 4.2, and 4.3, the results demonstrate the accuracy of certain FE tibia models in predicting the structural response of a human tibia to vibration. For free-free boundary conditions, the Bi-Material Model and Viscoelastic Model had the same medial-lateral bending mode value of 455 Hz, which fell within the experimental range (424-690 Hz) for a dry, excised tibia (Van Der Perre, 1983). This value of 455 Hz for both the Bi-Material and Viscoelastic Model was similar to the experimental resonance value of 476 Hz for a fresh, excised tibia reported by Christensen (1986). The Solid Model and the Hollow Model also had free-free bending modes of 320 Hz and 324 Hz that fell within the natural frequency range (310-392 Hz) for a fresh, excised tibia reported by Van Der Perre (1983)

For clamped-*z* conditions at the knee and ankle, the Bi-Material and Viscoelastic Model had medial-lateral bending modes of 404 Hz and 408 Hz, respectively. On the other hand, the Solid and Hollow Models had medial-lateral bending mode values of 805 Hz and 891 Hz for the constraints. The Solid and Hollow Model resonance values were approximately 140% and 160% greater than the experimental pinned-pinned bending mode for a wet, excised tibia (Christensen, 1986), whereas the Bi-Material and Viscoelastic values were within 20%. The more complex models (Bi-Material and Viscoelastic) were much closer in agreement with the pinned-pinned experimental value of 337 Hz for the wet, excised tibia (Christensen, 1986). This agreement suggests that the combination of cancellous bone at the proximal and distal regions of the tibia and linear viscoelastic properties for cortical and cancellous bone was more predictive of the structural resonances of a human tibia. Furthermore, the Bi-Material and Viscoelastic Models produced bending mode values that reproduced computational results reported by

Hight (1980), Hobatho (1991), and Lowet (1996). This further shows that the addition of cancellous bone and viscoelastic behavior accurately predicted the structural response of a human tibia. Therefore, the FE geometry, applied meshes, and material characteristics used in the more complex tibia models were verified during the calculation of the bending modes from the natural frequency analysis.

Discrepancies between FE tibia models and previously reported experimental values must be discussed. Parameters such as bone length, cross sectional moment of inertia, and mineral density will significantly affect the structural response of the tibia during vibration. In addition, parameters such as distance between supports, mode of vibration (hammer impact, modal analysis, etc.), and tissue preparation (dry, fresh, embalmed, etc.) will also significantly alter bending modes for the human tibia. The values listed in Tables 4.1, 4.2, 4.3 contain numerous values from different types of bones and experimentation. Therefore, these values were only provided as a reference to observe noticeable similarities and verify that the FE geometry of the tibia was accurately predicting the structural response of a human tibia.

## 4.2 Dynamic Responses

The direct steady-state dynamics (DSSD) procedure was used in each parametric study, shown in Table 3.4, to determine which components dominated the complex stiffness versus frequency response of the human tibia during vibration. Different material behaviors, constraints, and geometries were evaluated in these parametric studies to accurately simulate the experimental MRTA raw data or complex stiffness response of the tibia *in vivo*.

### 4.2.1 Dominant Parameters in the Frequency Domain

The four FE tibia models, Solid, Hollow, Bi-Material, and Viscoelastic were all analyzed under different proximal and distal tibia constraints. Figure 4.4 illustrates the dynamic responses for all four tibia models under each applied nodal constraint defined in Section 3.1.6.

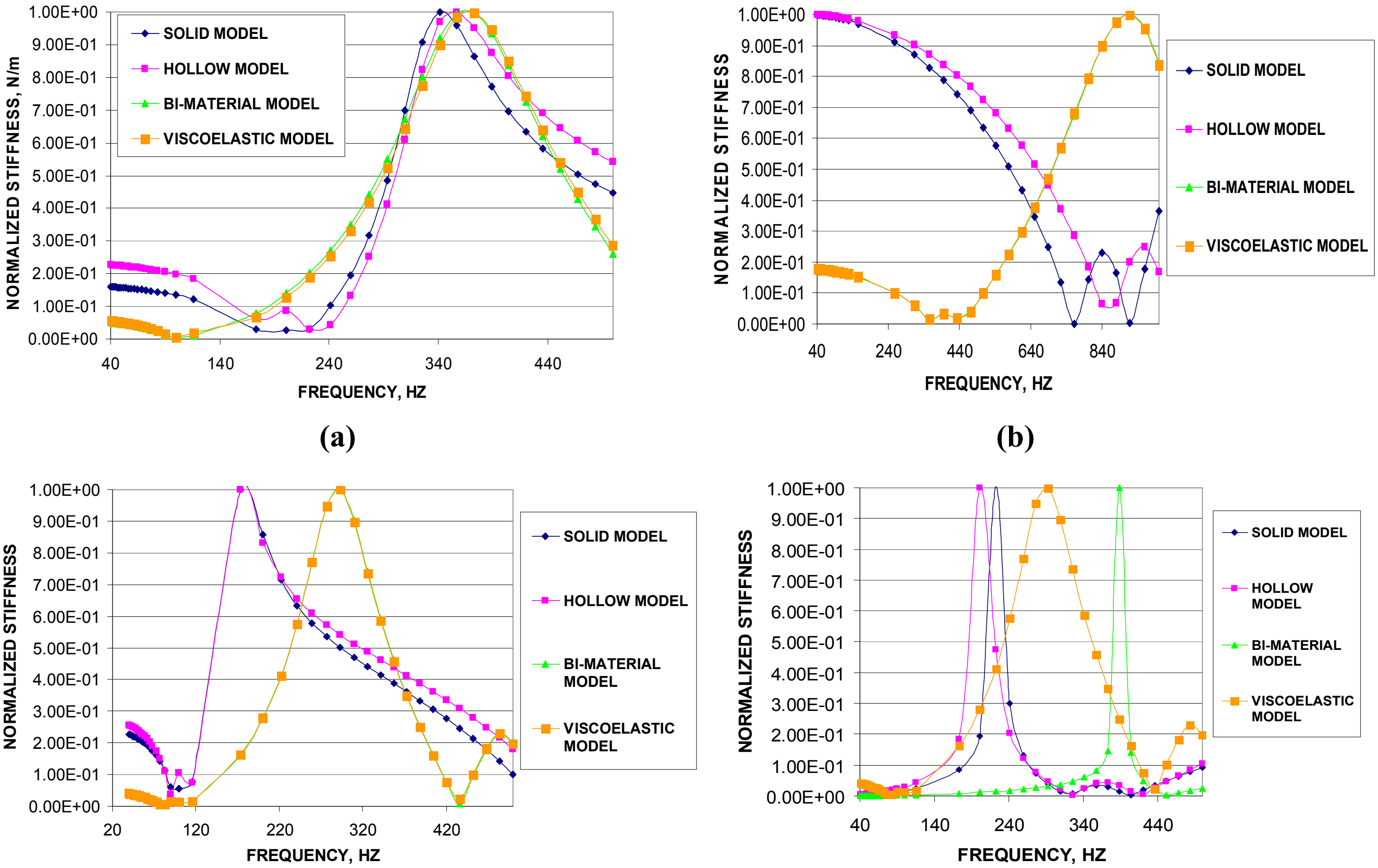

(a)

(b)

(c)

(d)

**Figure 4.4: Dynamic responses for tibia models for (a) clamped-*xy* BC (b) clamped-*z* (c) clamped-free (d) free-free**

In Figure 4.4, the steady-state responses were located at the beginning of the stiffness response curves near zero frequency for all dynamic responses. For each constraint except the free-free condition, the steady-state stiffness was much larger (order of magnitude) for the Solid and Hollow Models compared to the Bi-Material and

Viscoelastic Models. This observation can be attributed to the inclusion of the softer cancellous bone at the ends of the tibia in the Bi-Material and Viscoelastic Models, whereas the Solid and Hollow Models were made entirely of cortical bone, which is much stiffer than cancellous bone due to different levels of porosity. In addition, the Viscoelastic Model response curve was directly on top of the Bi-Material response curve during each applied constraint except the free-free condition.

Figure 4.5 shows the location of the maximum and minimum peaks in the frequency response for each FE tibia model under the clamped-*xy* constraint. Figure 4.5 also shows $\Delta$ or the frequency shift factor.

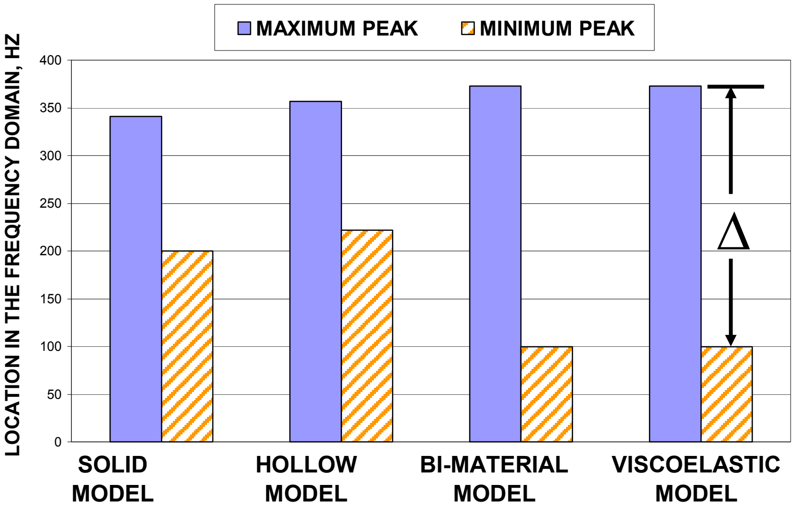

**Figure 4.5: Location of the maximum and minimum peaks in the frequency domain for each FE tibia model with pinned-xy boundary conditions**

The shift factor quantifies the distance between the maximum and minimum peaks in the frequency domain. This parameter can be used to quantify the effects of different complexities on the dynamic response of the tibia. For example, an increase in the shift factor equals a larger distance between maximum and minimum peaks or a broader response. A broader response curve in the frequency domain represents an increase in damping of the structure during vibration. For a decrease in the shift factor, the frequency response curve has a much sharper resonance representing a stiffer structure. Table 4.4 shows the shift factors for the response curves illustrated in Figure 4.5a for the clamped-*xy* constraint.

**Table 4.4: Shift factors for all FE models under the clamped-*xy* constraint**

| FE Model | Shift Factor, $\Delta$ (Hz) |
|---|---|
| Solid | 141 |
| Hollow | 135 |
| Bi-Material | 273 |
| Viscoelastic | 273 |

As shown in Figure 4.5a and Table 4.4, there was no difference in maximum and minimum peak location or shift factor between the Bi-Material and Viscoelastic Models. This suggests that viscoelasticity of cortical and cancellous bone has negligible effect in the frequency domain for the dynamic stiffness response of the tibia during vibration. The Bi-Material and Viscoelastic Models, however, did broaden the stiffness response curves by increasing the shift factor in comparison to the Solid and Hollow Models.

Since the location of maximum peaks (blue bar graphs in Figure 4.5) is very similar for all FE tibia models, the dominant component in the frequency domain during vibration of the tibia was the cortical shell geometry. The cortical shell geometry was constant for each FE tibia model; therefore, the location of the maximum value in the frequency domain was mostly dependent on the cortical shell geometry during vibrational testing. Adding the medullary canal and LVE properties to cancellous and cortical bone did not greatly spread the peak or shift the resonant frequency. Therefore, modeling of the cortical shell geometry must be accurate for effective FE simulation of the complex stiffness response measured by the MRTA experimental device.

### 4.2.2 Effects of Nodal Constraints

In review of the different proximal and distal constraints, there were noticeable effects from different constraints on the complex stiffness response. Figure 4.4 illustrates the effects of each constraint on the dynamic responses for all FE tibia models. The clamped-*z* BC shifted the resonances (maximum and minimum peaks) higher or to the right in the frequency domain. For example, the Bi-Material and Viscoelastic Models both had a maximum peak value at 918.7 Hz for the clamped-*z* constraint, but for the clamped-*xy* constraint (Figure 4.4a), these models had a maximum peak value at 373 Hz. The effect was even more magnified for the Solid and Hollow Models, whose maximum peak resonances were not noticeable when the frequency range was extended to 1000 Hz. Conversely, the clamped-free constraint or "cantilever" constraint shifted the resonances to lower values and produced a much sharper resonant peak (distance between minimum and maximum values) for the Solid and Hollow Models. As for the free-free boundary condition, only one maximum peak resonance was observed in the range of 200-400 Hz for all models. However, the clamped-*xy* constraint produced, maximum peak values for all models that fell within the range of 341 to 373 Hz, which closely fit within the experimental natural frequency range (310-392 Hz) for a human tibia reported by Van Der Perre (1983).

The percentage of constrained nodes at the proximal and distal tibia was investigated for the Viscoelastic Model. Figure 4.6 shows the effects of different percentages for the applied constraints at the surface nodes of the proximal and distal tibia.

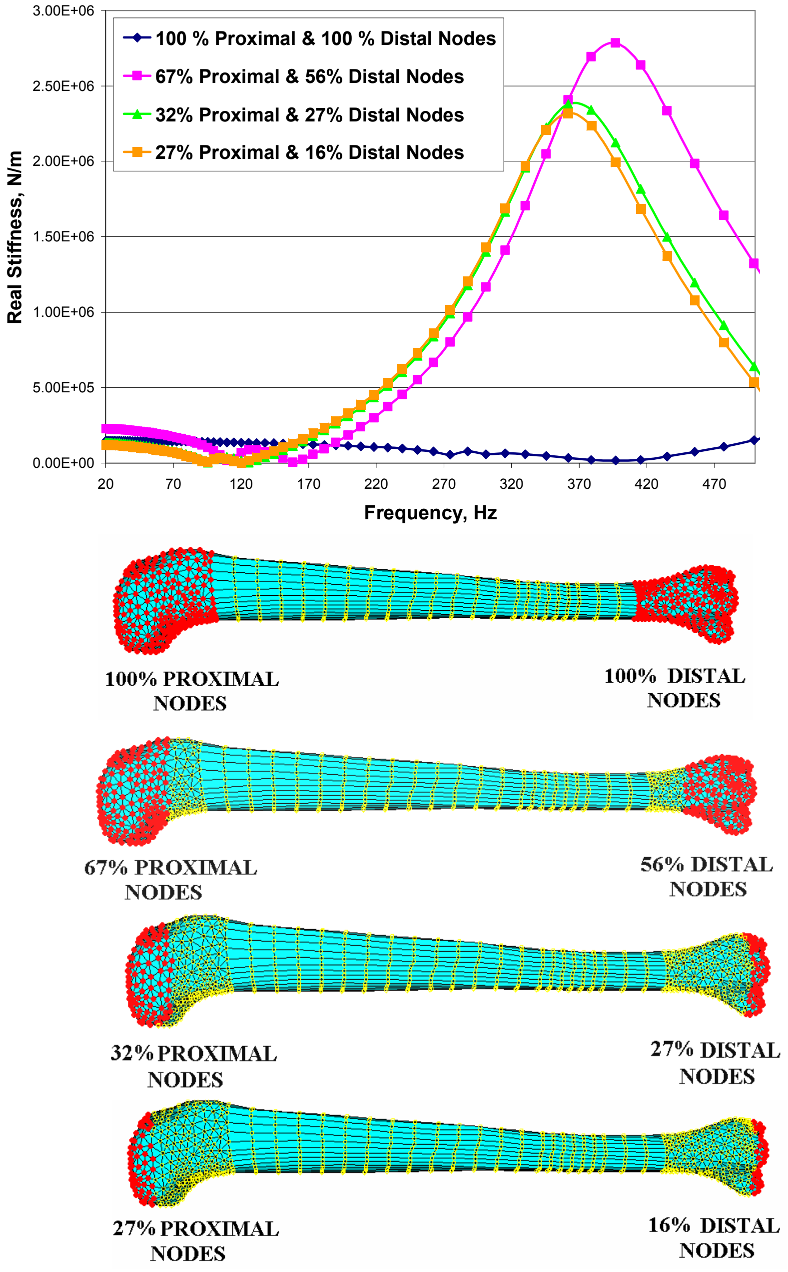

**Figure 4.6: Effects of constrained nodes at proximal and distal ends on the dynamic response of the Viscoelastic Model**

The percentage case with 67% of constrained proximal nodes and 56% of constrained distal nodes was taken to be the default constraint because this case was assumed to represent the proximal and distal regions where bending motion was restricted by anatomical structures such as connective tissue (ligaments and tendons) and muscles. The percentage of constrained nodes was evaluated to expose any error associated with the applied FE boundary conditions during the simulation of the MRTA stiffness versus frequency response. Figure 4.7 shows the maximum and minimum peaks in the frequency response for the Viscoelastic Model under different percentages of constrained nodes.

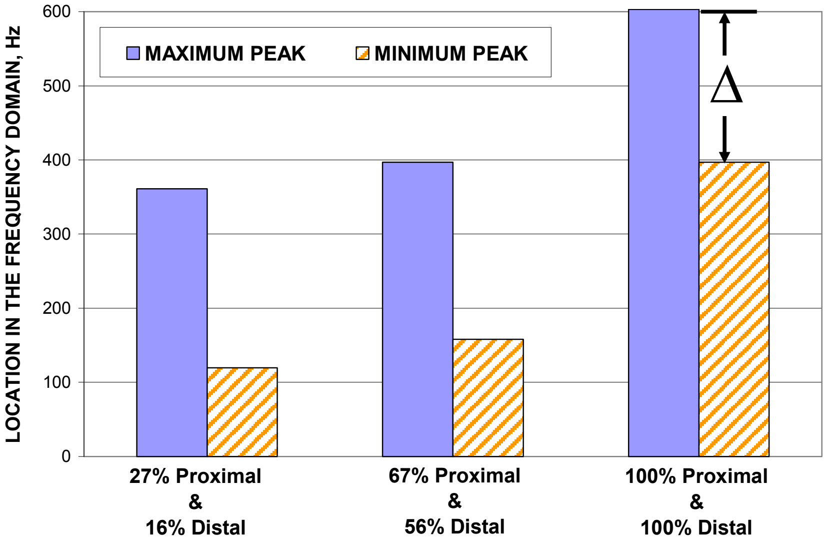

**Figure 4.7: Location of the maximum and minimum peaks for different percentages of constrained nodes**

In Figure 4.7, the 100% constrained case shifted the maximum and minimum peak values in the frequency domain to the right in comparison to the default case (67% & 56%). The 27%-16%, the 67%-56%, and the 100%-100% cases had shift factors of 241 Hz, 239 Hz, and 206 Hz, respectively. The shift factor was expected to decrease for the 100%-100% case because more constrained nodes limited the translational motion and decreased damping, thus creating a sharper resonance in the response curve. On the other hand, the case for 27% constrained proximal nodes and 16% constrained distal nodes increased the shift factor in comparison to the default case. As expected, a larger shift factor equates to a broader response curve suggesting more translational motion at the proximal and distal ends of the tibia during vibration. Therefore, the percentage of constrained nodes for the FE tibia models did affect the dynamic response of the FE tibia models during vibration. To eliminate any inherent error associated with constrained nodes, the default case (67% proximal and 56% distal) was applied to all subsequent parametric studies.

To further evaluate the effects of nodal constraints, the location and numbers of nodes at the proximal and distal tibia were examined. Figure 4.8 illustrates the dynamic responses of the Viscoelastic Model for different cases of constrained nodes at the posterior or bottom portion of the proximal and distal tibia.

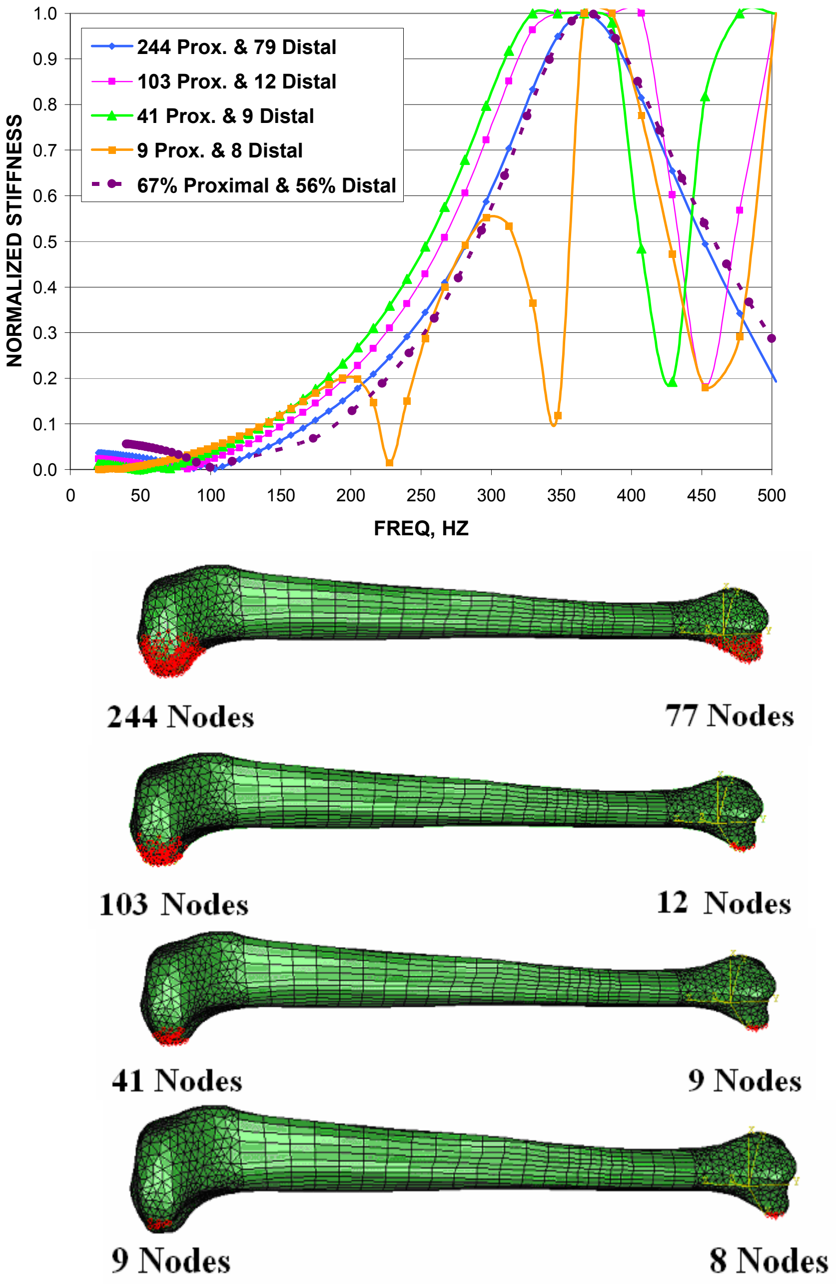

**Figure 4.8: Effects of constrained node location on the dynamic response of the viscoelastic model**

Figure 4.9 identifies the location of maximum and minimum peaks in the frequency domain for the dynamic response of the Viscoelastic Model with constrained nodes at the bottom portion of the tibia end regions.

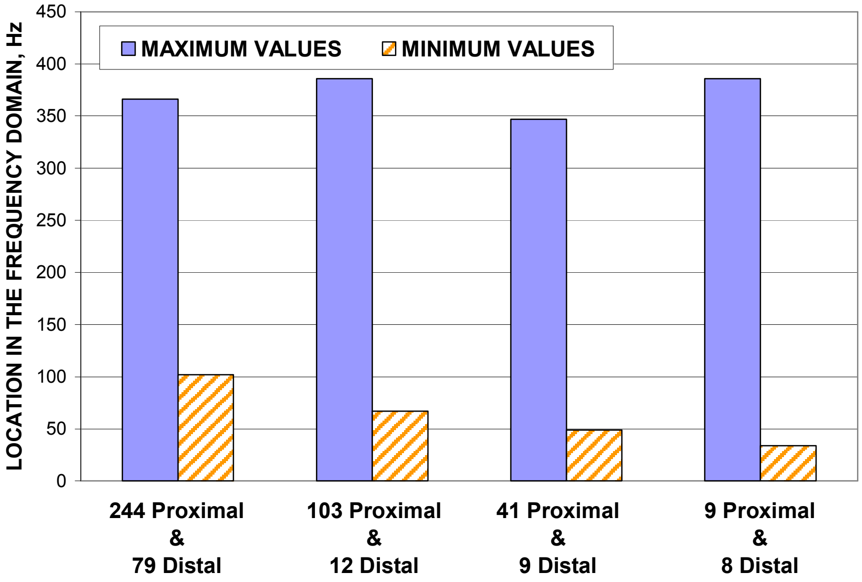

**Figure 4.9: Location of the maximum and minimum peaks for different numbers of constrained nodes at the bottom portion of the proximal and distal tibia**

It is apparent from Figure 4.8 and Figure 4.9 that the location for the maximum peaks was relatively the same for each case; therefore, the small differences among the maximum peak resonances suggest that the location of constrained nodes has a minimal effect on the stiffness response in the frequency domain. The number of constrained nodes, however, did show a significant effect on the minimum peak value in the frequency domain. When the number of constrained nodes was greatly reduced, there was more apparent displacement at the proximal and distal ends of the tibia due to multiple degrees of freedom for the FE tibia models. This is evident in Figure 4.8 by the increase in resonant peaks for the cases with very few constrained nodes. Therefore, a certain number of nodes must be constrained during the simulation of the MRTA technique to accurately determine the complex stiffness versus frequency response of a human tibia. This limitation was resolved by considering the default case (67% proximal and 56% distal) as ideal for nodal constraints at the proximal and distal tibia.

### 4.2.3 Effects of Soft Tissue

It was shown earlier that the dominant parameter in the stiffness versus frequency response was cortical shell geometry. This was the case for the FE tibia models with no soft tissue. However, the effects of soft tissue between the forcing probe and tibia were investigated using the Skin Model. The goal of the Skin Model was to better simulate the broadening of the response curve for the experimental MRTA raw data or complex stiffness.

Soft tissue characteristics were implemented into the FE simulations as a small "patch" of skin between the forcing probe and the tibia at the tibial crest. A thickness of 2mm was used to simulate the skin layer after the MRTA preload was applied to the limb during experimental testing of the tibia *in vivo*. Figure 4.10 illustrates the parametric study results for the soft tissue layer with material properties taken from the literature.

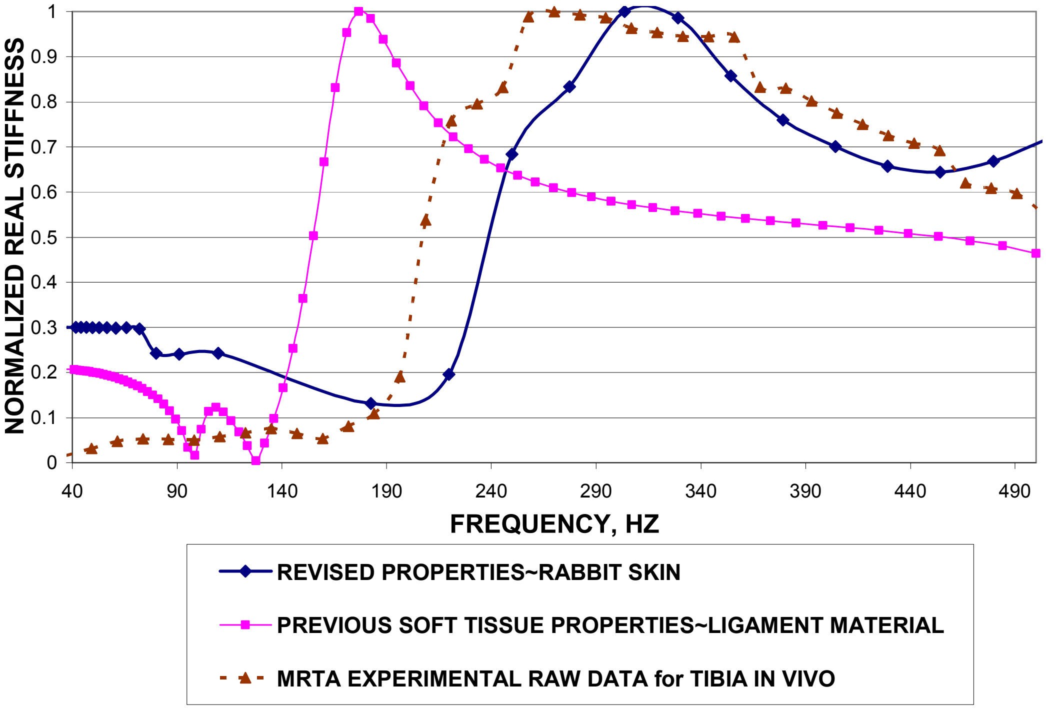

**Figure 4.10: Skin model response**

The first attempt at the skin layer had properties taken from Ambrosio (1998) for a polymeric material designed to mimic ligament soft tissue. The stiffness response curve did broaden out in comparison to the bone response, and the minimum and maximum peak values were shifted to lower values in the frequency domain suggesting that there is a contribution from this small skin layer to the overall dynamic response of the tibia. However, a second parametric study, the Revised Skin Model, revealed a more appropriate simulation of the experimental MRTA stiffness response by replacing the previous soft tissue properties with viscoelastic rabbit skin data taken from Periera (1991).

From the general shape of the curves, there is clear evidence in Figure 4.10 that the Revised Skin Model generated a dynamic response that was in close agreement with the experimental MRTA raw data for an *in vivo* tibia test. This suggests that the inclusion of a skin layer between the bone and forcing probe was necessary to accurately simulate the MRTA experimental technique for a tibial strength assessment.

The thickness of the skin layer was examined to observe any effects on the dynamic response of the tibia during vibration. Skin thicknesses of 0.5 mm, 2 mm, and 4 mm were analyzed with the DSSD procedure using the previous Skin Model (not the Revised Skin Mode). Figure 4.11 shows the effects of the different skin thicknesses.

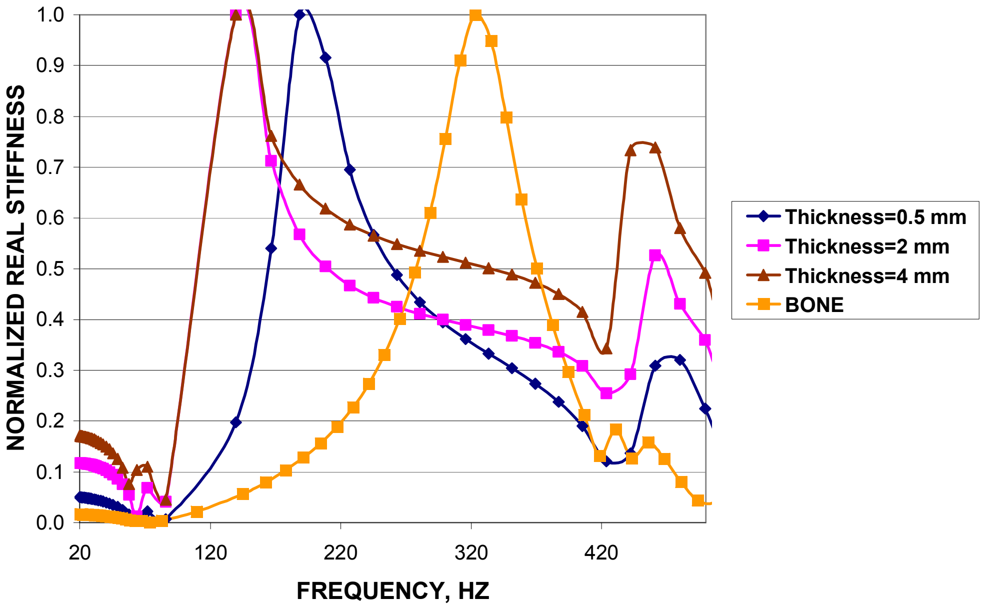

**Figure 4.11: Effects of skin layer thickness using previous soft tissue properties from ligament material**

When the thickness was increased, the skin response gradually broadened out in the frequency domain as expected. However, when the thickness of the skin layer was reduced, there was a response curve more indicative of the dynamic response due to bone only. Figure 4.11 shows that the skin layer of 0.5 mm has a shifted resonance (to the right) in the frequency domain and a much sharper resonant peak. These results suggest that with less and less skin, the dynamic response of the tibia is mainly due to the cortical and cancellous bone properties.

### 4.2.4 Effects of Spring-Dashpot End Conditions

Linear spring and dashpots were considered as alternate constraints for the tibia during vibration. Since the MRTA lumped parameter algorithms incorporated springs and dashpots, the stiffness and damping coefficients for linear springs and dashpots were added to the proximal and distal regions of the Revised Skin Model. Linear dashpot and spring stiffness coefficients for the proximal and distal tibia were taken from experimental MRTA output from the 12-parameter model (Callaghan, 2003). A spring stiffness of 1000 N/m and a damping coefficient of 100 N-s/m were applied to approximately 30 nodes at the posterior or bottom portion of both the proximal and distal tibia. Figure 4.12 represents the Revised Skin Model configuration and shows a plot for the dynamic response from the applied springs and dashpots.

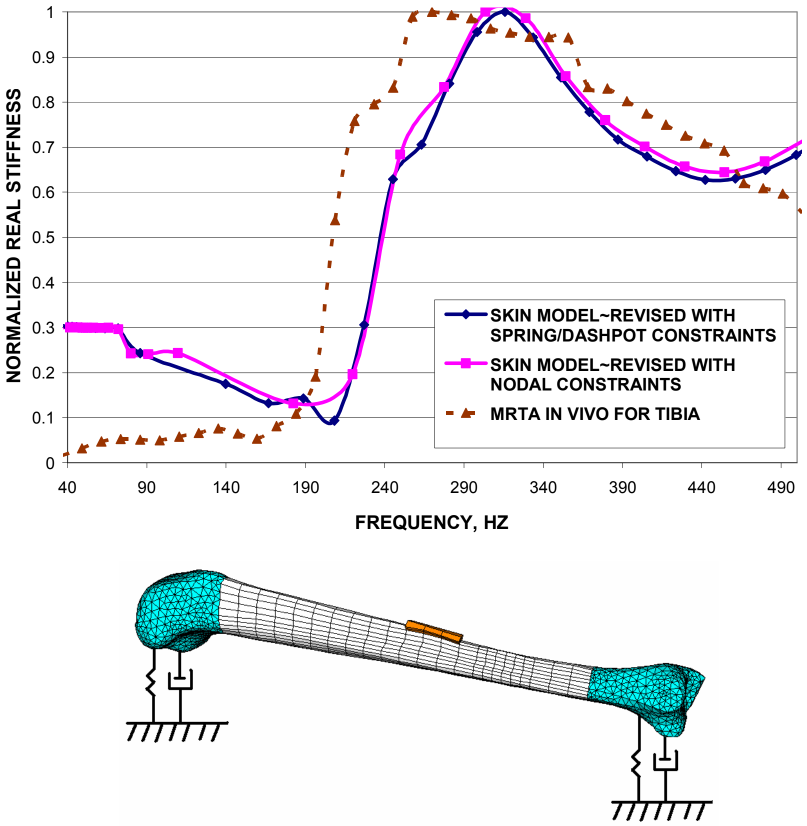

**Figure 4.12: Effects of replacing nodal constraints with spring/dashpot constraints for dynamic response of tibia**

The dynamic response curves show remarkable agreement between the spring-dashpot constraints and the previous nodal constraints for the Revised Skin Model. These results provide evidence that the spring-dashpot constraints are just as effective in simulating the stiffness versus frequency response for the experimental MRTA test of a human tibia.

### 4.2.5 Monitoring Cortical Bone Strength

The final parametric study (see Table 3.4) evaluated the effects of different cortical bone properties for the Viscoelastic Model. Cortical bone stiffness was either reduced or increased by 30%. The clamped-*xy* constraint and spring-dashpot constraints were applied to the Viscoelastic Model to monitor any changes in relation to the normal cortical bone response. Figures 4.13 and 4.14 illustrate the effects of different cortical bone properties in the frequency domain.

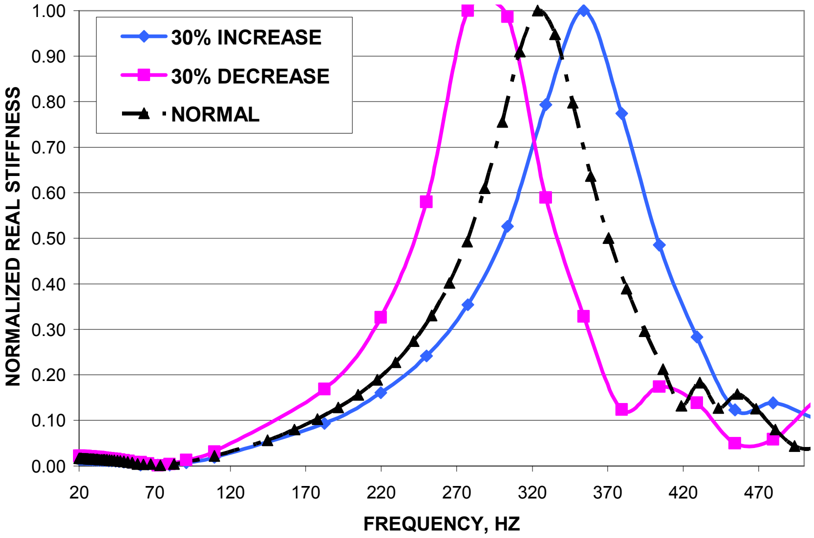

**Figure 4.13: Effects of changing cortical bone viscoelastic properties for viscoelastic model**

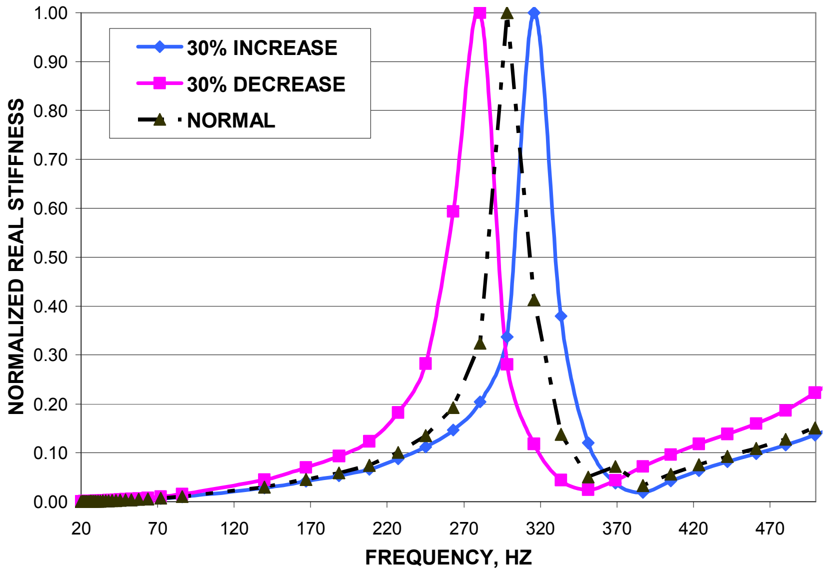

**Figure 4.14: Effects of changing cortical bone viscoelastic properties for spring/dashpot end conditions**

Figure 4.13 and Figure 4.14 illustrate that differences in dynamic response curves for weak, normal, and strong cortical bone properties were distinguishable. Figure 4.15 shows the location of maximum and minimum peak values for changes in cortical bone strength under nodal constraints and spring/dashpot conditions, respectively. Figure 4.16 illustrates the maximum peak locations for the spring/dashpot constraint for the Viscoelastic Model.

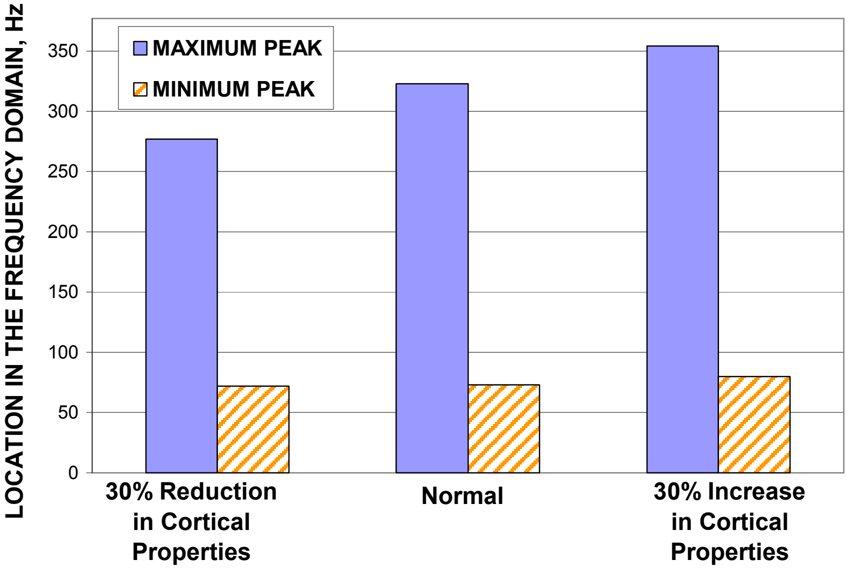

Figure 4.15: Location of maximum and minimum peak values for changes in cortical bone strength

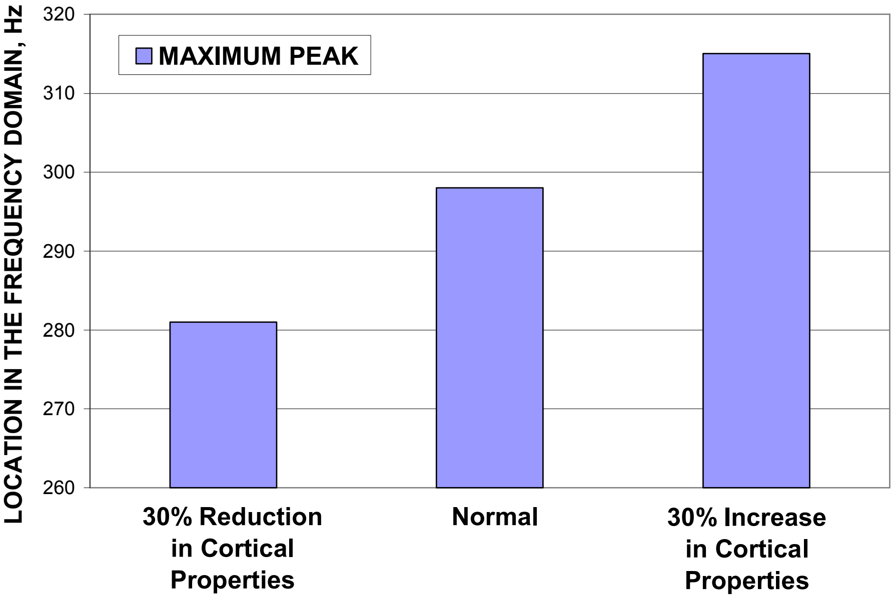

Figure 4.16: Location of maximum peak values for changes in cortical strength with spring-dashpot constraints

There is direct evidence in Figure 4.15 and Figure 4.16 that the DSSD procedure can detect changes in cortical bone strength in the frequency domain. For nodal constraints, the dynamic response for the Viscoelastic Model with weaker cortical bone had a maximum peak value at 277 Hz, whereas the normal Viscoelastic Model had a maximum peak resonance at 323 Hz. When the cortical bone strength was increased by 30%, the maximum peak value was increased to 354 Hz. In other words, a 30% increase in cortical stiffness created a 10% shift right for the maximum peak value in the frequency domain, whereas a 30% decrease generated a 14% shift left in the frequency domain. These changes were taken as extreme for human cortical bone stiffness; however, there was evidence that significant cortical strength changes can be monitored with the DSSD procedure developed during this first FE simulation of the MRTA test for a human tibia.

# 5. Conclusions

The computational methods and corresponding results in this thesis have lead to the first finite element (FE) simulation of the MRTA test of a human tibia. This simulation of the MRTA technique was developed through five FE models and three procedures (static, natural frequency, and DSSD), which were utilized to analyze various parametric studies. The research hypothesis was to identify dominant parameters in the complex stiffness response for the tibia under vibration. The external cortical shell geometry dominated the stiffness response of the tibia during simulated vibration. The addition of medullary canal and linear viscoelastic (LVE) cortical and cancellous bone properties did not greatly shift the resonance peaks in the frequency domain. The addition of the LVE skin layer broadened the peak response to more closely match the MRTA experimental response. Furthermore, three of the five research aims (see Section 2.3) developed in this thesis were supported by the results produced from the original FE methodology and analyses implemented into this thesis.

In review, the direct steady-state dynamics (DSSD) procedure in ABAQUS was validated with the computational and analytical analyses of prismatic and hollow-cylindrical beams. The agreement between analytical and computational results (see Appendix C) provided excellent evidence that the DSSD procedure accurately assessed the dynamic response of a structure to low frequency, low amplitude vibration. Therefore, the DSSD procedure was applied to FE tibia models to calculate the stiffness response in the frequency domain for numerous parametric studies.

Four finite element tibia models of increasing complexity were analyzed with the natural frequency analysis (ABAQUS) to investigate the structural and geometric accuracy of these models under different knee (proximal tibia) and ankle (distal tibia) constraints (see Section 3.1.6). After comparing these results to previous experimental and computational resonances of human tibiae, the resonances of the more complex models, the Bi-Material and Viscoelastic, were more accurate in simulating the bending modes of a human tibia. The dynamic response of the FE tibia models was dominated by the geometry of the cortical shell. In the frequency domain, the location of maximum peaks was relatively the same for all FE tibia models proving that there was very little effect from the addition of viscoelasticity properties for cortical and cancellous bone.

In addition, various boundary conditions were evaluated to expose any FE limitations in simulating the MRTA experimental constraints. There was direct evidence that different percentages of constrained nodes will affect the dynamic response of the tibia to vibration. More constrained nodes made the structural more rigid and decreased the shift factor resulting in a sharper resonance curve. On the other hand, fewer constrained nodes increased translational motion at the proximal and distal ends of the tibia generating a broader frequency response curve. Also, spring-dashpot constraints produced similar dynamic responses in relation to the constrained nodal methods. Therefore, the DSSD procedure exposed several boundary condition methods that could be manipulated to generate dynamic responses in close agreement with the MRTA experiment raw data; however, no single set of boundary conditions at the proximal and distal regions of the tibia was exposed that yielded an exact match to the experiment MRTA stiffness response.

Finally, inclusion of a skin layer into the FE simulation was the most effective in accurately simulating the experimental MRTA strength assessment for a human tibia. The skin layer between forcing probe and tibia generated a dynamic response with good agreement to the experimental response measured by the MRTA.

# 6. References

ABAQUS, *User's Manual. Version. 6.5*, Hibbit, Karlsson, 1992.

Adami, S., Gatti, D., Braga, V., Bianchini, D., Rossini, M. (1999). “Site-specific effects of strength training on bone structure and geometry of ultradistal radius in postmenopausal women.” *J Bone Miner Res*. 14**:**120-4.

Ambrosio, L., De Santis, R., Iannace, S., Netti, P.A., Nicolais, L. (1998). “Viscoelastic behavior of composite ligament prosthesis.” *J Biomed Mater Res* 42: 6–12.

An, Y.H., “Mechanical properties of bone,” pp. 41-63 in: An, Y.H., and Draughn, R.A., Eds., 2000, Mechanical Testing of Bone and the Bone-Implant Interface, CRC Press, Boca Raton.

An, Y.H., Barfield, W.R., Draughn, R.A. “Basic concepts of mechanical property measurement and bone biomechanics,” pp. 23-40 in: An, Y.H., and Draughn, R.A., Eds., 2000, Mechanical Testing of Bone and the Bone-Implant Interface, CRC Press, Boca Raton.

Anderson, D. (2005). An investigation of the mechanical implications of sacroplasty using the finite element models based on tomographic image data. M.S. Thesis, Virginia Tech.

Ask the White House. “Sean O’Keefe.” Jan. 7, 2003.
<http://www.whitehouse.gov/ask/20040107.html>

Bonucci, E., “Basic composition and structure of bone,” pp. 3-21 in: An, Y.H., and Draughn, R.A., Eds., 2000, Mechanical Testing of Bone and the Bone-Implant Interface, CRC Press, Boca Raton.

Burr, D. B. (2002). "Targeted and nontargeted remodeling." *Bone* 30(1): 2-4.

Callaghan, C. (2003). Reliability of tibial measurement with mechanical response tissue analysis. PhD Dissertation, Virginia Tech

Carter, D.R., Bouxsein, M.L., Marcus, R. (1992). “New approaches for interpreting projected bone densitometry data.” *J Bone Miner Res* 7(2):137-145.

Christensen, A.B., Ammitzboll, F., Dyrbye, C., Cornelissen, M., Cornelissen, P., Van Der Perre, G. (1986) “Assessment of tibia1 stiffness by vibration testing *in situ*--1. Identification of mode shapes in different supporting conditions.” *J. Biomechanics* 19: 53-60.

Currey, J.D. (1984). The Mechanical Adaptations of Bone, Princeton University Press, Princeton, NJ.

Djokoto, C. C. (2002). The optimization of a mechanical response tissue analyzer (MRTA) and a descriptive comparison with dual energy X-ray absorptiometry and quantitative ultrasound. M.S. Thesis, University of Toronto.

Dong, X.N., Yeni, Y.N., Les, C.M., Fyhrie, D.P. (2004). "Effects of end boundary conditions and specimen geometry on the viscoelastic properties of cancellous bone measured by dynamic mechanical analysis." *J Biomed Mater Res* 68A: 573–583.

Garner, E., Lakes, R.S., Lee, T., Swan, C., Brand, R. (2000). "Viscoelastic dissipation in compact bone: Implications for stress-induced fluid flow in bone." *J. Biomech Eng* 122: 166-172.

Glimcher, M.J., "Composition, structure, and organization of bone and other mineralized tissues and the mechanisms of calcification." in: Greep, R.O. and Astwood, E.B., Eds., 1976, Handbook of Physiology: Endocrinology, American Physiology Society, Washington, D.C.

Herbert, W.G., Steele, C.R., Nickols-Richardson, S.M., Ramp, W.K., Wootten, D.F., Miller, L.E., Callaghan, C.E. (2004) Poster: "Effects of isokinetic muscular strength training on tibial bending stiffness and BMD in young women." *American Society for Bone and Mineral Research.*

Hight, T.K., Piziali, R.L, Nagel, D.A. (1980). "Natural frequency analysis of a human tibia" *J. Biomechanics* 13: 139-47.

Hobatho, M.C, Darmana, R., Pastor, P., Barrau, J.J., Laroze, S., Morucci, J.P. (1991). "Development of a 3-D FE model of a human tibia using experimental modal analysis." *J. Biomechanics* 24 (6): 371-83.

Hudelmaier, M., Kuhn, V., Lochmuller, E.M., Well, H., Priemel, M., Link, T.M., Eckstein, F. (2004). "Can geometry-based parameters from pQCT and material parameters from quantitative ultrasound (QUS) improve the prediction of radial bone strength over that by bone mass (DXA)? *Osteoporosis Int.* 15: 375:381.

Khan, K. (2001). *Physical activity and bone health*. Champaign, IL, Human Kinetics.

Kiebzak, G.M., Box, J.H., Box, P. (1999). "Decreased ulnar bending stiffness in osteoporotic caucasian women." *Clinical Densitometry* 2: 143-152.

Kroger, H., Huopio, J., Honkanen, R., Tuppurainen, M., Puntila, E., Alhava, E., Saarikoski, S. (1995). "Prediction of fracture risk using axial bone mineral density in a perimenopausal population: a prospective study." *J Bone Miner Res*, 10(2), 302-306.

Jarvinen, T.L., Kannus, P., Sievanen, H. (1999). "Have the DXA-based exercise studies seriously underestimated the effects of mechanical loading on bone?" *J. Bone Miner Res* 14(9): 1634-5.

Jurist, J.M. (1970a). “In vivo determination of the elastic response of bone I: method of ulnar resonant frequency determination.” *Phys Med Biol* 15(3):417-26.

Jurist, J.M. (1970b), “In vivo determination of the elastic response of bone II: method of ulnar resonant frequency in osteoporotic, diabetic, and normal Subjects.” *Phys Med Biol* 15(3):427-34.

Lakes, R.S. (1982). “Dynamical study of couple stress effects in human compact bone.” *J. Biomech Eng* 104: 6-11.

Liang, M.T.C., Arnaud, S.B., Steele, C.R., Hatch, P., Moreno, A. (2005) “Ulnar and tibial bending stiffness as an index of bone strength in synchronized swimmers and gymnasts.” *Eur J Appl Physiol* 94: 400–407.

Lochmuller, E.M., Burklein, D., Kuhn, V., Glaser, C., Muller, R., Gluer, C.C., Eckstein, F. (2002). “Mechanical Strength of the thoracolumbar spine in the elderly: prediction from *in situ* dual-energy x-ray absorptiometry, quantitative computed tomography (QCT), upper and lower limb peripheral QCT, and quantitative ultrasound.” *Bone* 31 (1): 77-84.

Lochmuller, E.M., Muller, R., Kuhn, V., Lill, C.A., Eckstein, F. (2003). “Can novel clinical densitometric techniques replace or improve DXA in prediction of bone strength in osteoporosis at the hip and other skeletal sites?” *Amer. Society for Bone and Mineral Research* 18: 906-912.

Martin, R.B. (1991). "Determinants of the mechanical properties of bones." *J Biomech* 24(Suppl. 1): 79-88.

Martin, R.B., Burr, D.B. (1989). Structure, function, and adaptation of compact bone New York: Raven Press.

Miller, L.E. (2003). Reliability and validity of mechanical response tissue analysis in composite and human tibiae. Ph.D. Thesis, Virginia Polytechnic Institute and State University.

Munch, S., Shapiro, S. (2006). “The silent thief: osteoporosis and women’s health care across the life span.” *Health and Social Work*, 31.1: 44.

Oganov, V.S., Grigor'ev A.I., Voronin, L.I. (1992). “Bone mineral density in cosmonauts after flights lasting 4.5-6 months on the Mir orbital station.” *Aviakosm Ekolog Med* 26:20-4.

Orsini, L.S., Rousculp, M.D., Long, S.R., Wang, S. (2005). “Health care utilization and expenditures in the United States: a study of osteoporosis-related fractures.” *Osteoporosis Int* 16: 359-371.

Pereira, J., Mansour, J.M., Davis, B.R. (1991). “Dynamic Measurement of the Viscoelastic Properties of Skin.” *J. Biomech* 24: 157-162

Posner, A.S., “Bone mineral and the mineralization process,” in: Peck, W.A., Ed., 1987, Bone and Mineral Research, Vol. 5, Elsevier Science Publishers, Amsterdam.

Roberts, S.G., Hutchinson, T., Arnaud, S.B., Kiratli, B.J., Martin, R.B., Steele, C.R. (1996). “Noninvasive determination of bone mechanical properties using vibration response: a refined model and validation *in vivo*.” *J Biomech* 29 (1): 91-98.

Sasaki, N. “Viscoelastic properties of bone and testing methods,” pp. 329-348 in: An, Y.H., and Draughn, R.A., Eds., 2000, Mechanical Testing of Bone and the Bone-Implant Interface, CRC Press, Boca Raton.

Seeman, E. (2002). “Pathogenesis of bone fragility in women and men.” Lancet, 359 (9320), 1841-1850.

Siu, W.S., Qin, L., Leung, K.S. (2003). “pQCT bone strength index may serve as a better predictor than bone mineral density for long bone breaking strength.” *Bone Mineral Metabolism* 21: 316-322.

Snowdon, J.C. (1968) Vibration and Shock in Damped Mechanical Systems. Wiley & Sons, Inc., New York.

Steele, C.R., Zhou, L.J., Guido, D., Marcus, R., Heinrichs,W.L., Cheema, C. (1988). "Noninvasive determination of ulnar stiffness from mechanical response: in vivo comparison of stiffness and bone mineral content in humans." *J Biomech Eng* 110(2): 87-96.

Steele, C. R. (2006). Personal communication.

Stromsoe, K., Hoiseth, A., Alho, A., Kok, W.L. (1995). “Bending strength of the femur in relation to non-invasive bone mineral assessment.” *J. Biomechanics* 28 (7): 857-861.

Svendsen, O.L., Hassager, C., Skodt, V., Christiansen, C. (1995). “Impact of soft tissue on in vivo accuracy of bone mineral measurements in the spine, hip, and forearm: a human cadaver study.” *J Bone Miner Res* 10(6): 868-873.

Thorne, R. A. (2000). Mechanical response tissue analysis: inter- and intra-trial reliability in assessing bending stiffness of the human tibia in college aged women. M.S. Thesis, Virginia Tech.

Van der Perre, G., Van Audekercke, R., Martens, M., Mulier, J.C. (1983). “Identification of *in-vivo* vibration modes of human tibia by modal analysis.” *J. Biomech. Eng.* 105: 244-8.

Viceconti, M, *International Congress on Computational Bioengineering*, M. Doblaré, et al, Eds., Zaragoza, Sept. 24-26, (2003) <http://www.tecno.ior.it/VRLAB/researchers/repository/BEL_repository.html>

Weber, M., Hasler, P., and Gerber, H., 1993, “Insufficiency Fractures of the Sacrum, Twenty Cases and Review of the Literature,” *SPINE*, 18(16): 2507-2512.

Wolff, J. (1986). The law of bone remodelling. Berlin; New York, Springer-Verlag.

World Health Organization (1994). *Assessment of fracture risk and its application to screening for postmenopausal osteoporosis: report of a WHO study group*. Paper presented at the WHO Technical Report Series, Geneva.

Young, DR, Thompson GA, Orne D. (1976). “In vivo determination of mechanical properties of the human ulna by means of mechanical impedance tests: experimental results and improved mathematical model.” *Med Biol Eng* 14 (3): 252-62.

Young, D.R., Niklowitz, W.J., Steele, C.R. (1983). “Tibial changes in experimental disuse osteoporosis in the monkey.” *Calcified Tissue Int* 35(3): 304-8.

Zioupos P., Smith, C.W., An, Y.H., “Factors affecting mechanical properties of bone,” pp. 65-86 in: An, Y.H., and Draughn, R.A., Eds., 2000, Mechanical Testing of Bone and the Bone-Implant Interface, CRC Press, Boca Raton.

# Appendix A: Linear Viscoelasticity

For dynamic loading of bone, the input is usually a harmonically oscillating force that is assumed to be taking place long enough that the oscillation can be considered to be “steady state”, implying that there are no “transients” from the initiation of the loading. Equation A.1 defines the complex form for an input function of force.

$$F^* = F_o e^{i(\omega t)} \qquad \textbf{(A.1)}$$

Since the loading pattern in the direct steady state dynamics (DSSD) procedure uses the form in Equation A.1, frequency-dependent moduli for the elastic modulus (E) and the shear modulus (G) can be inputted into the FE simulation to better represent the material behavior of the tibia as well as the soft tissue. Equation A.2 and A.3 shows the frequency-dependent complex elastic modulus and shear modulus, respectively.

$$E^*(i\omega) = E^{'}(\omega) + iE^{''}(\omega) \quad (Young's\ Modulus) \qquad \textbf{(A.2)}$$

$$G^*(i\omega) = G^{'}(\omega) + iG^{''}(\omega) \quad (Shear\ Modulus) \qquad \textbf{(A.3)}$$

The storage moduli, $E^{'}(\omega)$ *and* $G^{'}(\omega)$, are a measure of the amount of energy stored in the material during dynamic testing whereas the loss moduli, $E^{''}(\omega)$ *and* $G^{''}(\omega)$, reflect the amount of energy dissipated from the material. The loss tangent, defined in Equation A.4, is the ratio of loss modulus to storage modulus, and it represents the amount of damping in the material being tested.

$$tan\,\delta = \frac{Loss\ Modulus}{Storage\ modulus} = \frac{E^{''}(\omega)}{E^{'}(\omega)} = \frac{G^{''}(\omega)}{G^{'}(\omega)} \qquad \textbf{(A.4)}$$

The frequency-dependent storage modulus, loss moduli, and loss tangent for cortical bone (Lakes, 1982; Garner, 2000), cancellous bone (Dong, 2003), soft tissue (Ambrosio, 1998), and rabbit skin (Periera, 1991) were taken from the literature. All materials were assumed to be incompressible, and the shear modulus was related to the elastic modulus by Equation A.5.

$$G = \frac{E}{2(1+\nu)} \qquad \textbf{(A.5)}$$

The values of the loss and storage moduli for cortical bone, cancellous bone, soft tissue, and rabbit skin are tabularized and plotted in the frequency domain in Figures A.1 through A. 4, respectively. The values for cancellous bone in the literature were only given in the range of 1-20 Hz, therefore, an extrapolation of the data to 500 Hz was conducted for cancellous bone. Power law equations were fitted to the experimental viscoelastic data and extrapolated to 500 Hz. Equations A.6 and A.7 define the power law equations used to extrapolate the experimental cancellous bone data.

$$G'(\omega) = 3.50E7(\omega^{0.0747}) \qquad \textbf{(A.6)}$$

$$G''(\omega) = 3.90E6(\omega^{-0.041}) \qquad \textbf{(A.7)}$$

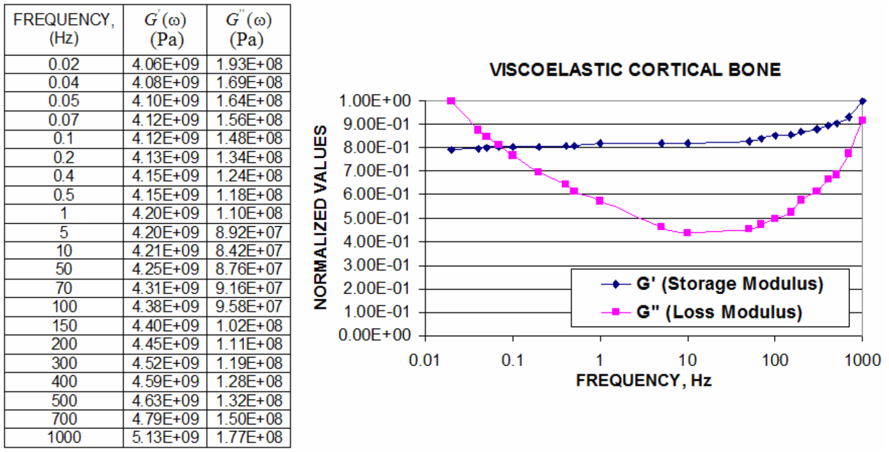

| FREQUENCY, (Hz) | $G'(\omega)$ (Pa) | $G''(\omega)$ (Pa) |
|---|---|---|
| 0.02 | 4.06E+09 | 1.93E+08 |
| 0.04 | 4.08E+09 | 1.69E+08 |
| 0.05 | 4.10E+09 | 1.64E+08 |
| 0.07 | 4.12E+09 | 1.56E+08 |
| 0.1 | 4.12E+09 | 1.48E+08 |
| 0.2 | 4.13E+09 | 1.34E+08 |
| 0.4 | 4.15E+09 | 1.24E+08 |
| 0.5 | 4.15E+09 | 1.18E+08 |
| 1 | 4.20E+09 | 1.10E+08 |
| 5 | 4.20E+09 | 8.92E+07 |
| 10 | 4.21E+09 | 8.42E+07 |
| 50 | 4.25E+09 | 8.76E+07 |
| 70 | 4.31E+09 | 9.16E+07 |
| 100 | 4.38E+09 | 9.58E+07 |
| 150 | 4.40E+09 | 1.02E+08 |
| 200 | 4.45E+09 | 1.11E+08 |
| 300 | 4.52E+09 | 1.19E+08 |
| 400 | 4.59E+09 | 1.28E+08 |
| 500 | 4.63E+09 | 1.32E+08 |
| 700 | 4.79E+09 | 1.50E+08 |
| 1000 | 5.13E+09 | 1.77E+08 |

Figure A. 1: Cortical bone values for frequency dependent material behavior

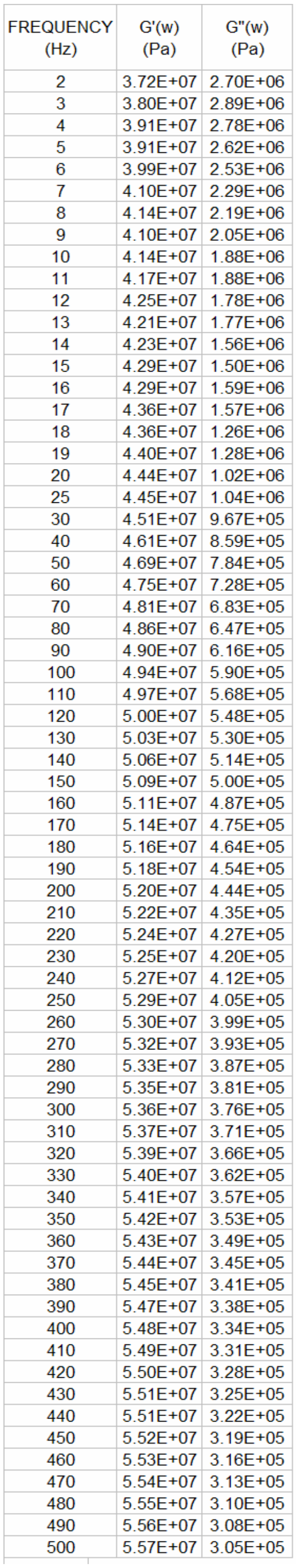

| FREQUENCY (Hz) | G'(w) (Pa) | G"(w) (Pa) |
|---|---|---|
| 2 | 3.72E+07 | 2.70E+06 |
| 3 | 3.80E+07 | 2.89E+06 |
| 4 | 3.91E+07 | 2.78E+06 |
| 5 | 3.91E+07 | 2.62E+06 |
| 6 | 3.99E+07 | 2.53E+06 |
| 7 | 4.10E+07 | 2.29E+06 |
| 8 | 4.14E+07 | 2.19E+06 |
| 9 | 4.10E+07 | 2.05E+06 |
| 10 | 4.14E+07 | 1.88E+06 |
| 11 | 4.17E+07 | 1.88E+06 |
| 12 | 4.25E+07 | 1.78E+06 |
| 13 | 4.21E+07 | 1.77E+06 |
| 14 | 4.23E+07 | 1.56E+06 |
| 15 | 4.29E+07 | 1.50E+06 |
| 16 | 4.29E+07 | 1.59E+06 |
| 17 | 4.36E+07 | 1.57E+06 |
| 18 | 4.36E+07 | 1.26E+06 |
| 19 | 4.40E+07 | 1.28E+06 |
| 20 | 4.44E+07 | 1.02E+06 |
| 25 | 4.45E+07 | 1.04E+06 |
| 30 | 4.51E+07 | 9.67E+05 |
| 40 | 4.61E+07 | 8.59E+05 |
| 50 | 4.69E+07 | 7.84E+05 |
| 60 | 4.75E+07 | 7.28E+05 |
| 70 | 4.81E+07 | 6.83E+05 |
| 80 | 4.86E+07 | 6.47E+05 |
| 90 | 4.90E+07 | 6.16E+05 |
| 100 | 4.94E+07 | 5.90E+05 |
| 110 | 4.97E+07 | 5.68E+05 |
| 120 | 5.00E+07 | 5.48E+05 |
| 130 | 5.03E+07 | 5.30E+05 |
| 140 | 5.06E+07 | 5.14E+05 |
| 150 | 5.09E+07 | 5.00E+05 |
| 160 | 5.11E+07 | 4.87E+05 |
| 170 | 5.14E+07 | 4.75E+05 |
| 180 | 5.16E+07 | 4.64E+05 |
| 190 | 5.18E+07 | 4.54E+05 |
| 200 | 5.20E+07 | 4.44E+05 |
| 210 | 5.22E+07 | 4.35E+05 |
| 220 | 5.24E+07 | 4.27E+05 |
| 230 | 5.25E+07 | 4.20E+05 |
| 240 | 5.27E+07 | 4.12E+05 |
| 250 | 5.29E+07 | 4.05E+05 |
| 260 | 5.30E+07 | 3.99E+05 |
| 270 | 5.32E+07 | 3.93E+05 |
| 280 | 5.33E+07 | 3.87E+05 |
| 290 | 5.35E+07 | 3.81E+05 |
| 300 | 5.36E+07 | 3.76E+05 |
| 310 | 5.37E+07 | 3.71E+05 |
| 320 | 5.39E+07 | 3.66E+05 |
| 330 | 5.40E+07 | 3.62E+05 |
| 340 | 5.41E+07 | 3.57E+05 |
| 350 | 5.42E+07 | 3.53E+05 |
| 360 | 5.43E+07 | 3.49E+05 |
| 370 | 5.44E+07 | 3.45E+05 |
| 380 | 5.45E+07 | 3.41E+05 |
| 390 | 5.47E+07 | 3.38E+05 |
| 400 | 5.48E+07 | 3.34E+05 |
| 410 | 5.49E+07 | 3.31E+05 |
| 420 | 5.50E+07 | 3.28E+05 |
| 430 | 5.51E+07 | 3.25E+05 |
| 440 | 5.51E+07 | 3.22E+05 |
| 450 | 5.52E+07 | 3.19E+05 |
| 460 | 5.53E+07 | 3.16E+05 |
| 470 | 5.54E+07 | 3.13E+05 |
| 480 | 5.55E+07 | 3.10E+05 |
| 490 | 5.56E+07 | 3.08E+05 |
| 500 | 5.57E+07 | 3.05E+05 |

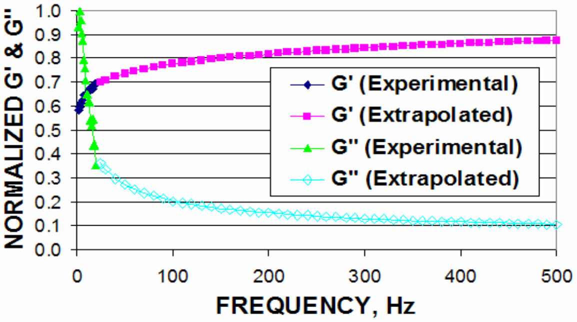

Figure A. 2: Cancellous bone values for frequency dependent material behavior

| FREQUENCY, (HZ) | $G^{'}(\omega)$ (Pa) | $G^{''}(\omega)$ (Pa) |
|---|---|---|
| 0.1 | 2.83E+06 | 8.99E+05 |
| 10.1 | 1.05E+07 | 2.44E+06 |
| 20.1 | 1.17E+07 | 2.67E+06 |
| 30.1 | 1.23E+07 | 2.80E+06 |
| 40.1 | 1.28E+07 | 2.90E+06 |
| 50.1 | 1.32E+07 | 2.97E+06 |
| 60.1 | 1.35E+07 | 3.03E+06 |
| 70.1 | 1.38E+07 | 3.08E+06 |
| 80.1 | 1.40E+07 | 3.13E+06 |
| 90.1 | 1.42E+07 | 3.17E+06 |
| 100.1 | 1.43E+07 | 3.20E+06 |
| 110.1 | 1.45E+07 | 3.23E+06 |
| 120.1 | 1.46E+07 | 3.26E+06 |
| 130.1 | 1.48E+07 | 3.29E+06 |
| 140.1 | 1.49E+07 | 3.31E+06 |
| 150.1 | 1.50E+07 | 3.34E+06 |
| 160.1 | 1.51E+07 | 3.36E+06 |
| 170.1 | 1.52E+07 | 3.38E+06 |
| 180.1 | 1.53E+07 | 3.40E+06 |
| 190.1 | 1.54E+07 | 3.42E+06 |
| 200.1 | 1.55E+07 | 3.43E+06 |
| 210.1 | 1.56E+07 | 3.45E+06 |
| 220.1 | 1.57E+07 | 3.46E+06 |
| 230.1 | 1.57E+07 | 3.48E+06 |
| 240.1 | 1.58E+07 | 3.49E+06 |
| 250.1 | 1.59E+07 | 3.51E+06 |
| 260.1 | 1.59E+07 | 3.52E+06 |
| 270.1 | 1.60E+07 | 3.53E+06 |
| 280.1 | 1.61E+07 | 3.55E+06 |
| 290.1 | 1.61E+07 | 3.56E+06 |
| 300.1 | 1.62E+07 | 3.57E+06 |
| 310.1 | 1.62E+07 | 3.58E+06 |
| 320.1 | 1.63E+07 | 3.59E+06 |
| 330.1 | 1.63E+07 | 3.60E+06 |
| 340.1 | 1.64E+07 | 3.61E+06 |
| 350.1 | 1.64E+07 | 3.62E+06 |
| 360.1 | 1.65E+07 | 3.63E+06 |
| 370.1 | 1.65E+07 | 3.64E+06 |
| 380.1 | 1.66E+07 | 3.65E+06 |
| 390.1 | 1.66E+07 | 3.66E+06 |
| 400.1 | 1.67E+07 | 3.66E+06 |
| 410.1 | 1.67E+07 | 3.67E+06 |
| 420.1 | 1.67E+07 | 3.68E+06 |
| 430.1 | 1.68E+07 | 3.69E+06 |
| 440.1 | 1.68E+07 | 3.70E+06 |
| 450.1 | 1.68E+07 | 3.70E+06 |
| 460.1 | 1.69E+07 | 3.71E+06 |
| 470.1 | 1.69E+07 | 3.72E+06 |
| 480.1 | 1.70E+07 | 3.72E+06 |
| 490.1 | 1.70E+07 | 3.73E+06 |
| 500.1 | 1.70E+07 | 3.74E+06 |
| 510.1 | 1.71E+07 | 3.75E+06 |
| 520.1 | 1.71E+07 | 3.75E+06 |
| 530.1 | 1.71E+07 | 3.76E+06 |
| 540.1 | 1.72E+07 | 3.76E+06 |
| 550.1 | 1.72E+07 | 3.77E+06 |
| 560.1 | 1.72E+07 | 3.78E+06 |
| 570.1 | 1.72E+07 | 3.78E+06 |
| 580.1 | 1.73E+07 | 3.79E+06 |
| 590.1 | 1.73E+07 | 3.79E+06 |
| 600.1 | 1.73E+07 | 3.80E+06 |
| 610.1 | 1.74E+07 | 3.80E+06 |
| 620.1 | 1.74E+07 | 3.81E+06 |

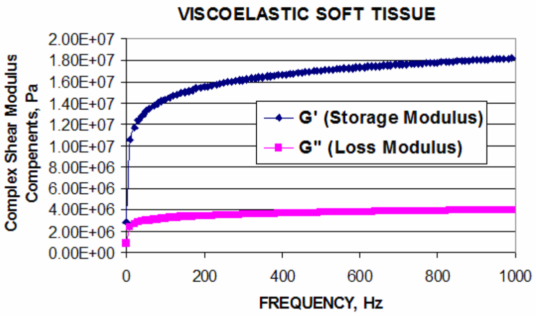

Figure A. 3: Soft tissue values for frequency dependent material behavior

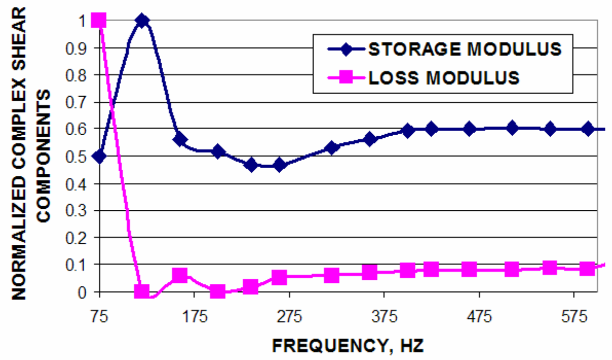

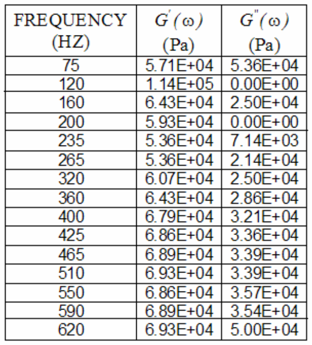

| FREQUENCY (HZ) | $G^{'}(\omega)$ (Pa) | $G^{''}(\omega)$ (Pa) |
|---|---|---|
| 75 | 5.71E+04 | 5.36E+04 |
| 120 | 1.14E+05 | 0.00E+00 |
| 160 | 6.43E+04 | 2.50E+04 |
| 200 | 5.93E+04 | 0.00E+00 |
| 235 | 5.36E+04 | 7.14E+03 |
| 265 | 5.36E+04 | 2.14E+04 |
| 320 | 6.07E+04 | 2.50E+04 |
| 360 | 6.43E+04 | 2.86E+04 |
| 400 | 6.79E+04 | 3.21E+04 |
| 425 | 6.86E+04 | 3.36E+04 |
| 465 | 6.89E+04 | 3.39E+04 |
| 510 | 6.93E+04 | 3.39E+04 |
| 550 | 6.86E+04 | 3.57E+04 |
| 590 | 6.89E+04 | 3.54E+04 |
| 620 | 6.93E+04 | 5.00E+04 |

**Figure A. 4: Rabbit skin values for frequency dependent material behavior**

Before these frequency dependent values were inputted into the FE models, mathematical calculations were made to convert the shear storage and loss moduli into the real and imaginary components of the nondimensional shear variable that ABAQUS required for tabular input of viscoelastic material behavior (ABAQUS User's Manual, v6.5). Equations A.8 and A.9 define the conversions applied to the experimental values for cortical and cancellous bone, soft tissue, and the rabbit skin. $G_\infty$ represents the long-term shear modulus which comes from the linear elastic material constants for bone or soft tissue.

$$\omega\Re(g^*) = \frac{G^{''}(\omega)}{G_\infty} \qquad \textbf{(A.8)}$$

$$\omega \Im(g^*) = 1 - \frac{G'(\omega)}{G_\infty} \qquad \textbf{(A.9)}$$

# Appendix B: Vibration Theory

1) **Transverse Vibration Equations**: Refer to Snowdon (1968) for derivation of all equations.

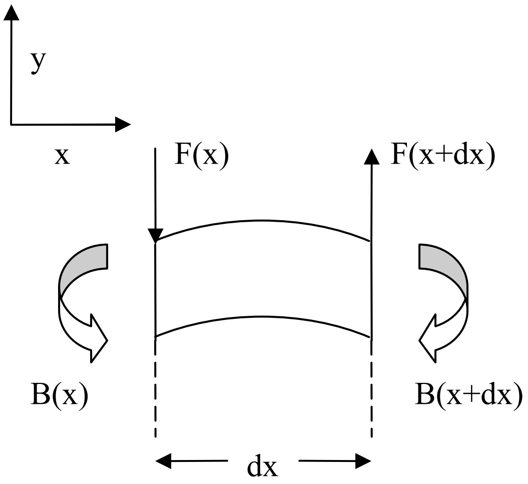

**Figure B. 1: Sinusoidally varying forces and bending moments acting on elementary segment of a beam in transverse vibration**

2) The wave equation that describes the transverse vibration of internally damped Bernoulli-Euler beam is written as:

$$\frac{\partial^4 y}{\partial x^4} = -\left(\frac{\rho}{E_w^* I}\right)\frac{\partial^2 y}{\partial t^2} \qquad \textbf{(B.1)}$$

3) The progressive wave solution for the wave equation (Equation A.1) can be determined by:
    a. Assuming that the sinusoidally varying beam displacement, y, may be written in the form:

$$y = y^*(x)e^{jwt}$$

$$\textit{where } y^*(x) \textit{ is a function of } x \textit{ only}$$

    b. The wave equation (Equation A.1), then becomes:

$$\frac{\partial^4 y}{\partial x^4} = \left(n^*\right)^4 y$$

$$\frac{d^4 y^*(x)}{dx^4} - (n^*)^4 y^*(x) = 0 \qquad \textbf{(B.2)}$$

    c. The progressive wave solution to Equation A.2 is:

$$\frac{d^4 y^*(x)}{dx^4} - (n^*)^4 y^*(x) = 0$$

$$y^*(x) = A^* e^{B^* x}$$

$$y^*(x) = (a^* e^{-jn^* x} + b^* e^{jn^* x} + c^* e^{-n^* x} + d^* e^{n^* x}) \tag{B.3}$$

*where a,b,c,d are arbitrary constants that depend on boundary conditions*

&

$$\left(n^*\right)^4 = \frac{\omega^2 \rho}{E_\omega^* r^2}$$

4) From Equation A.3, the closed form, standing-wave solution can be written as follows:

$$y^*(x) = (a^* e^{-jn^* x} + b^* e^{jn^* x} + c^* e^{-n^* x} + d^* e^{n^* x})$$

$$\begin{bmatrix} e^{\pm n^* x} = (\cosh(n^* x) \pm \sinh(n^* x)) \\ \text{and} \\ e^{\pm jn^* x} = (\cos(n^* x) \pm j\sin(n^* x)) \end{bmatrix} \tag{B.4}$$

$$y = \left(P^* \cosh(n^* x) + Q^* \cos(n^* x) + R^* \sinh(n^* x) + S^* \sin(n^* x)\right) e^{jwt}$$

*where $P^*$, $Q^*$, $R^*$, $S^*$ are arbitrary constants that depend on boundary conditions*

a. The expressions for the gradient, bending moment, and shearing force that act on elementary segments of a beam are directly related to the first, second, or third partial derivatives of y with respect to x. These expressions are:

$$y = \left(P^* \cosh(n^* x) + Q^* \cos(n^* x) + R^* \sinh(n^* x) + S^* \sin(n^* x)\right) e^{jwt}$$

$$\frac{\partial y}{\partial x} = n^* \left(P^* \sinh(n^* x) - Q^* \sin(n^* x) + R^* \cosh(n^* x) + S^* \cos(n^* x)\right) e^{jwt}$$

$$\frac{\partial^2 y}{\partial x^2} = (n^*)^2 \left(P^* \cosh(n^* x) - Q^* \cos(n^* x) + R^* \sinh(n^* x) - S^* \sin(n^* x)\right) e^{jwt} \tag{B.5}$$

$$\frac{\partial^3 y}{\partial x^3} = (n^*)^3 \left(P^* \sinh(n^* x) + Q^* \sin(n^* x) + R^* \cosh(n^* x) - S^* \cos(n^* x)\right) e^{jwt}$$

5) **Transverse Vibration:-Analytical Solution for Simply Supported Beam:**
    a. A simply supported beam has its ends hinged in such as way that they remain free to pivot about their points of support without constraint.
    b. At ends, displacement and bending moment are zero.
    c. When a beam is driven at its midpoint by a sinusoidally varying force, as shown in Figure A.2, only the symmetrical beam modes are excited (origin at center of beam).

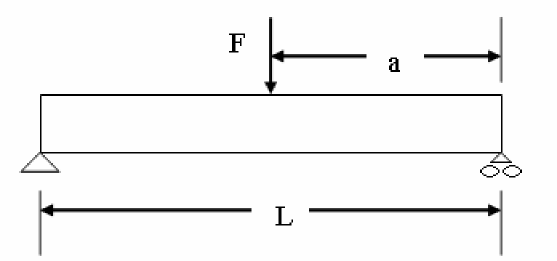

**Figure B. 2: Representation for simply supported beam**

d. The boundary conditions for this simply supported beam are:

$$BC \ \ at \ center \ of \ beam: \left(\frac{\partial y}{\partial x}\right)_{x=0} = 0$$

$$BC \ \ right \ hand \ end \ of \ beam:$$

$$(y)_{x=a} = 0 \qquad \textbf{(B.6)}$$

$$\left(\frac{\partial^2 y}{\partial x^2}\right)_{x=a} = 0$$

e. Plugging in boundary conditions to the appropriate expressions (Equations A.3-A.5), it can be shown that:

$$R^* = -S^*$$

$$and$$

$$F_o = -2E^* I (n^*)^3 (R^* - S^*)$$

$$F_o = \left(\frac{2w^2 M_b}{n^* a}\right) S^* \quad where \ M_b = mass \ of \ beam \qquad \textbf{(B.7)}$$

$$\&$$

$$P^* \cos h(n^* a) + Q^* \cos(n^* a) = S^* (\sin h(n^* a) - \sin(n^* a))$$

$$P^* \cos h(n^* a) - Q^* \cos(n^* a) = S^* (\sin h(n^* a) + \sin(n^* a))$$

f. Solving these equations simultaneously, we get:

$$P^* = \left(\frac{\sinh(n^* a)}{\cosh(n^* a)}\right) S^*$$

$$Q^* = -\left(\frac{\sin(n^* a)}{\cos(n^* a)}\right) S^* \qquad \textbf{(B.8)}$$

g. Since S* can be determined from Equation A.7, the displacement at any point x along the beam may be written as :

$$y = \frac{F_o (n^* a)}{2w^2 M_b}\left[\left(\frac{\sinh(n^* a)}{\cosh(n^* a)}\right)\cosh(n^* x) - \left(\frac{\sin(n^* a)}{\cos(n^* a)}\right)\cos(n^* x) - \sinh(n^* x) + \sin(n^* x)\right] e^{jwt} \qquad \textbf{(B.9)}$$

h. The center of beam displacement (x=0) is written as:

$$y = \frac{F_o(n^*a)}{2w^2M_b}\left[\left(\frac{\sinh(n^*a)\cos(n^*a) - \cosh(n^*a)\sin(n^*a)}{\cosh(n^*a)\cos(n^*a)}\right)\right]e^{jwt} \qquad \textbf{(B.10)}$$

# Appendix C: FE Validation

The prismatic or square FE beam consisted of 481 hexagonal, linear elastic solid elements with 776 nodes while the hollow-cylindrical beam had 4,800 hexagonal elements with 6,150 nodes. Figure C.1 depicts the two beam models used in the validation of each FE analysis (static, natural frequency, and DSSD).

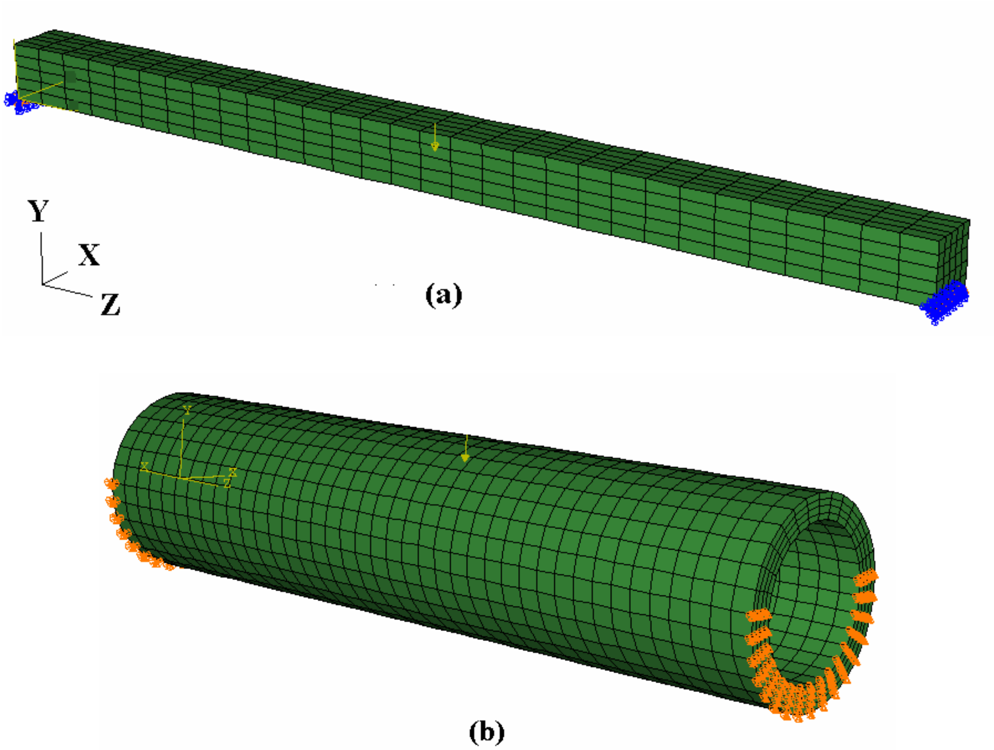

(a)

(b)

**Figure C. 1: Finite element validation models (a) prismatic solid beam (blue arrows show constrained nodes) (b) hollow, cylindrical beam (orange arrows show constrained nodes)**

Based on beam theory, analytical solutions for a simply-supported prismatic beam and hollow-cylindrical beam in vibration were derived and compared to the computational results for the two FE beam models. Figure 3.9 depicts the prismatic and hollow-cylindrical beam representations for the steady-state analytical solution, which is located in Appendix D.

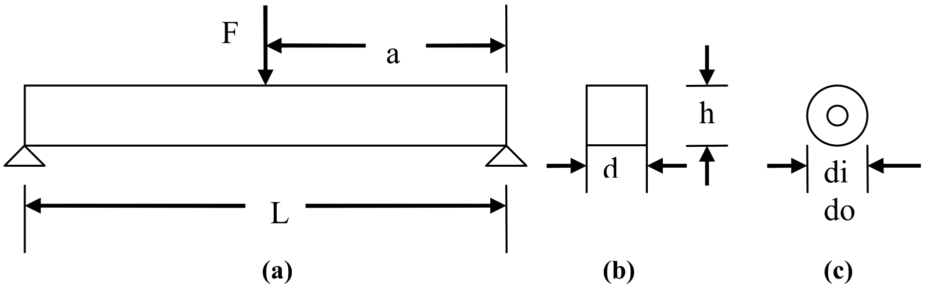

**Figure C. 2: Analytical beam representation (a) simply supported beam (b) solid, prismatic (square) cross section (c) hollow-cylindrical cross section**

To ensure validation, simply-supported boundary conditions were applied to both the prismatic and hollow beams with selected nodes constrained (no translation) in the *x-, y-,* and *z*-directions at one beam end and constrained in the *x*- and *y*- directions at the other beam end (refer to Figure C.1). For the square beam, the nodes at the bottom edge of each end were constrained while the nodes on the bottom half of the tube edges were constrained for the hollow-cylindrical beam (refer to Figure C.1). In the both simulations, the prismatic and hollow cylindrical beams were made of aluminum and considered to be force-driven at the beam's midpoint by a 100 N force.

ABAQUS (v6.5) and MATLAB (v6.1) were used in all validation analyses with units calculated in meters. Table C.1 lists the material properties for aluminum implemented into the FE and analytical analyses. Table C.2 and Table C.3 show the geometric parameters used in the FE and analytical simulations for prismatic and hollow-cylindrical beams, respectively.

**Table C.1: Aluminum material properties**

| | |
|---|---|
| E | 70 GPa |
| v | 0.33 |
| density | 2700 kg/m$^3$ |

**Table C.2: Prismatic beam geometric parameters (refer to Figure C.2b)**

| | |
|---|---|
| $Length,\ L$ | 0.35 meters |
| $Distance\ to\ midpoint,\ a$ | 0.175 m |
| $Height,\ h$ | 0.02 m |
| $Cross\ Sectional\ Area\ (CSA) = d * h$ | 0.0004 m$^2$ |
| $Radius\ of\ gyration,\ r = \frac{d}{\sqrt{12}}$ | 0.005774 m |
| $Area\ Moment\ of\ Inertia,\ I = CSA * r^2$ | 1.33E-8 m$^4$ |

**Table C.3: Hollow, cylindrical beam geometric parameters (refer to Figure C.2c)**

| | |
|---|---|
| $Length,\ L$ | 0.35 meters |
| $Distance\ to\ midpoint,\ a$ | 0.175 m |
| $Inner\ diameter, d_i$ | 0.06 m |
| $Outer\ diameter, d_o$ | 0.08 m |
| $Cross\ Sectional\ Area\ (CSA) = \pi * (rad_{outer}{}^2 - rad_{inner}{}^2)$ | 0.0022 m$^2$ |
| $r = \frac{(d_i{}^2 + d_o{}^2)^{1/2}}{4}$ | 0.025 m |
| $I = Area * r^2 = \pi * (rad_{outer}{}^2 - rad_{inner}{}^2) * r^2$ | 1.37E-6 m$^4$ |

## C.1 Prismatic Beam Results

The natural frequencies, maximum deflection, and dynamic response of the analytical prismatic beam were compared to the bending modes, maximum static displacement, and stiffness response of the 3-D finite element prismatic beam. The natural frequencies for the analytical prismatic beam were calculated from Equation C.1 for simply supported constraints.

$$f\,(Hertz) = \frac{j^2}{2}\frac{\pi}{L^2}\sqrt{\frac{E_o I}{\mu}} \quad for\ j = 1,2,3,4.... \qquad \textbf{(C.1)}$$

Table C.4 compares the natural frequencies of the analytical prismatic beam to the bending modes of the FE model. The FE prismatic beam had several degrees of freedom with a bending mode in the vertical plane (*y*-) and one in the horizontal plane (*x*-), whereas the analytical beam only had a single degree of freedom in the vertical (y-) plane). Figure C.1 depicts the first and second bending modes for the FE prismatic beam in the vertical direction.

**Table C.4: Prismatic beam validation results**

| Modes | Natural Frequencies for Analytical Beam (Hz) | FE Computational Bending Modes (Hz) (Vertical Plane Only) |
|---|---|---|
| 1 | 376.5 | 392.9 |
| 2 | 1505.9 | 1495.4 |
| 3 | 3388.4 | 3397.4 |
| 4 | 6023.8 | 5826.2 |
| 5 | 9412.1 | 8725.1 |

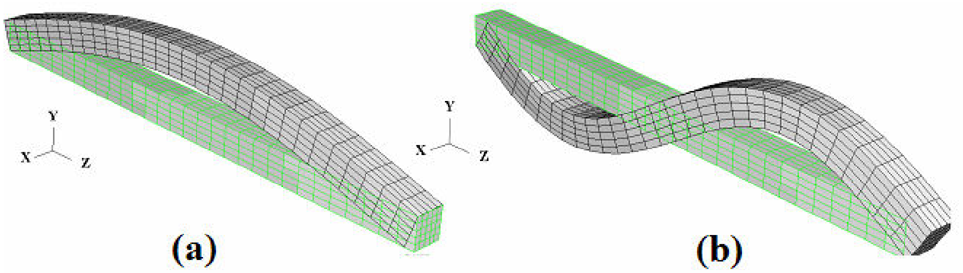

**Figure C. 3: FE computational bending modes for FE prismatic beam (plotted against un-deformed beam) (a) mode 1-vertical plane (b) mode 2-vertical plane**

The maximum deflection for the analytical prismatic beam was calculated using Equation C.2, which is derived from Euler-Bernoulli beam theory for a simply supported beam. This maximum deflection value, shown in Table C.5, was compared to the maximum static displacement of the FE prismatic beam during the static FE analysis.

$$Maximum\,Deflection,\ \delta_T = \frac{PL^3}{48EI} \qquad \textbf{(C.2)}$$

**Table C.5: Static results for prismatic beam**

| Analytical Maximum Deflection (meters) | FE Maximum Displacement (meters) |
|---|---|
| 9.57E-5 | 9.0E-5 |

In Table C.5, the difference between the two values was approximately 6%. In the case of the FE prismatic beam, there are shear and compression deflections associated with the static loading of the beam. These deflections, however, are neglected in Equation C.2 for a simply supported prismatic beam due to the assumptions in the Euler-Bernoulli beam theory. Therefore, a small difference in deflections between the analytical and computational FE results was expected.

The dynamic response due to sinusoidal varying forces was also calculated in the frequency domain using the direct steady-state dynamics procedure (DSSD). For the analytical prismatic beam, derived equations for the force-driven vibration (Appendix A) at the midpoint of the beam were simulated in MATLAB (v6.1). The DSSD procedure in ABAQUS was used to vibrate the FE prismatic beam over a range of frequencies. The stiffness response of each beam was calculated from the ratio between the dynamic forcing function and displacement response. Figure C.2 and Figure C.3 illustrate the dynamic analysis results for absolute displacement and stiffness responses, respectively.

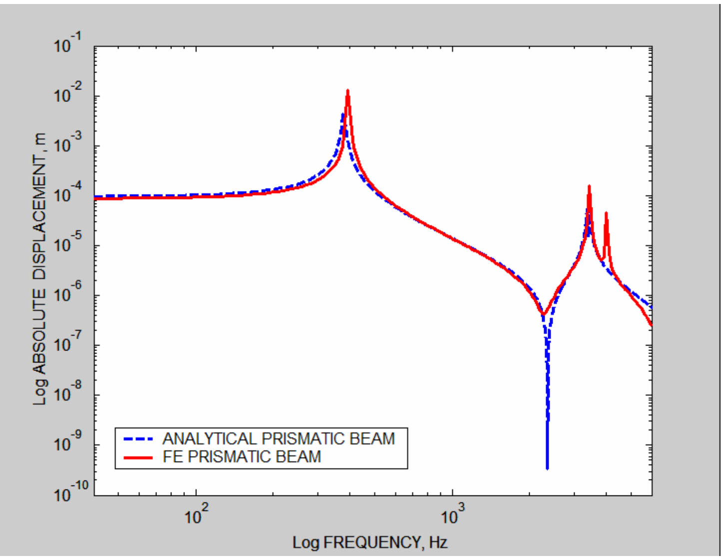

**Figure C. 4: Absolute displacement vs. frequency for analytical and FE prismatic beams**

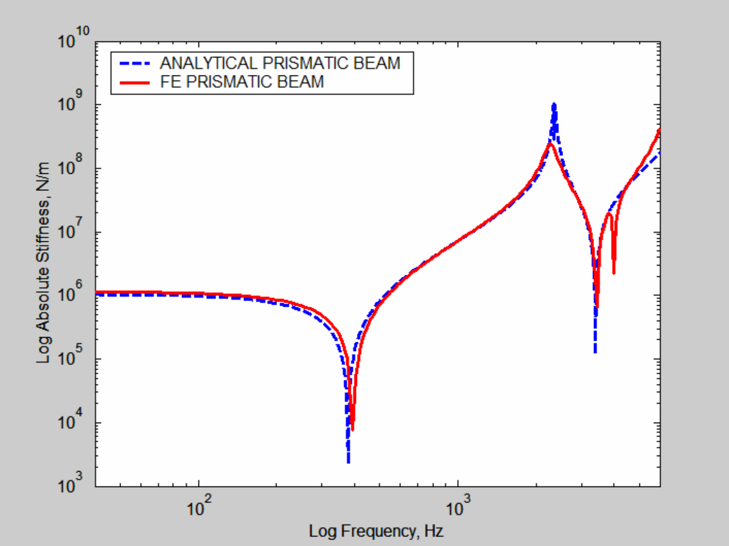

**Figure C. 5: Absolute stiffness vs. frequency for analytical and FE prismatic beams**

The discrepancies between response curves are related to the varying degrees of freedom between the analytical and FE prismatic models. At higher frequencies, the bending modes in different planes are evident for the FE model but do not exist for the analytical beam. However, the DSSD procedure does generate a frequency response curve very similar to the analytically derived vibration of a simply-supported prismatic beam. This similarity provides validation for the DSSD procedure and suggests its suitability in accurately determining the frequency response for a structure such as a prismatic beam. In addition, the relatively low error (<6%) for the static and natural frequencies procedures validates these finite element analyses as acceptable testing methods for the human tibia FE models.

## *C.2 Hollow-Cylindrical Beam Results*

The same FE experimental analyses (static, natural frequency, and DSSD) were evaluated for the hollow-cylindrical beam. The results of each analysis were once again compared to a derived solution for an analytical hollow-cylindrical beam. The bending modes in the vertical plane and horizontal plane were also observed for the FE hollow-cylindrical beam. Table C.6 compares the first and second natural frequencies (calculated from Equation C.1) for the analytical hollow-cylindrical beam to the FE hollow-cylindrical bending modes.

**Table C.6: Hollow cylindrical beam validation results**

| Modes | Natural Frequencies for Analytical Beam (Hz) | FE Computational Bending Modes (Hz) (Vertical Plane Only) |
|---|---|---|
| 1 | 1631.91 | 1365.9 |
| 2 | 6527.64 | 6041.9 |

The maximum displacement for the FE hollow-cylindrical beam from the static FE analysis was 1.0E-6 meters while the maximum deflection for the analytical hollow-cylindrical beam was 9.284E-7 meters. The percent error between the analytical and FE static solution was approximately 8.1%. Figure C.4 and Figure C.5 show the similarity in dynamic responses (displacement and stiffness) between the FE beam and analytical beam. This similarity in dynamic response and the relatively low error from the static and natural frequency analyses further emphasize the ability of these FE procedures to accurately predict the structural response of any beam regardless of geometry. The small error associated with the static and natural frequency analyses can be associated with the difference in degrees of freedom between FE model and analytical validation model.

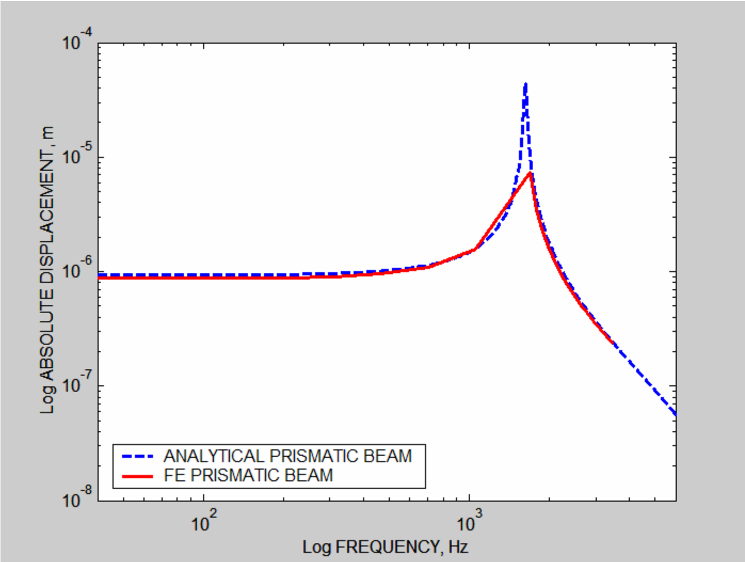

**Figure C. 6: Absolute displacement vs. frequency for analytical and FE hollow-cylindrical beams**

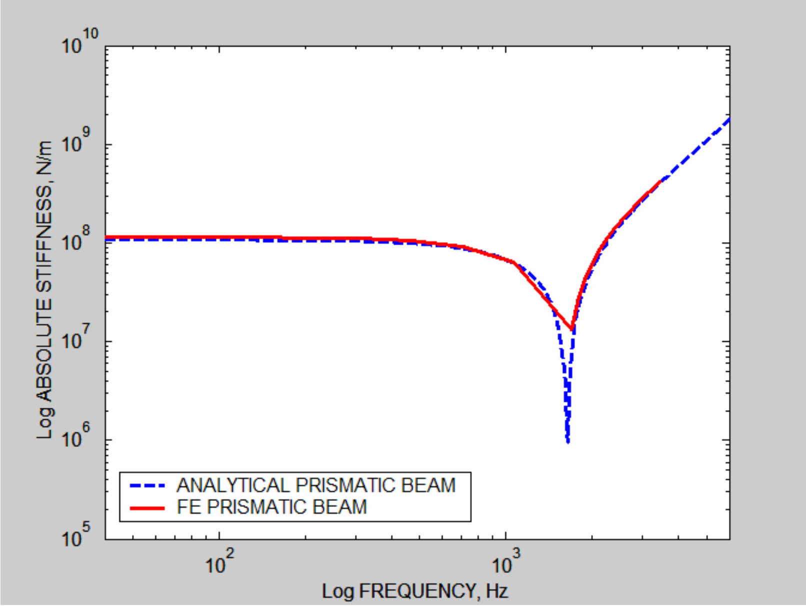

**Figure C. 7: Absolute stiffness vs. frequency for analytical and FE hollow-cylindrical beams**

# Appendix D: Parametric Study Results

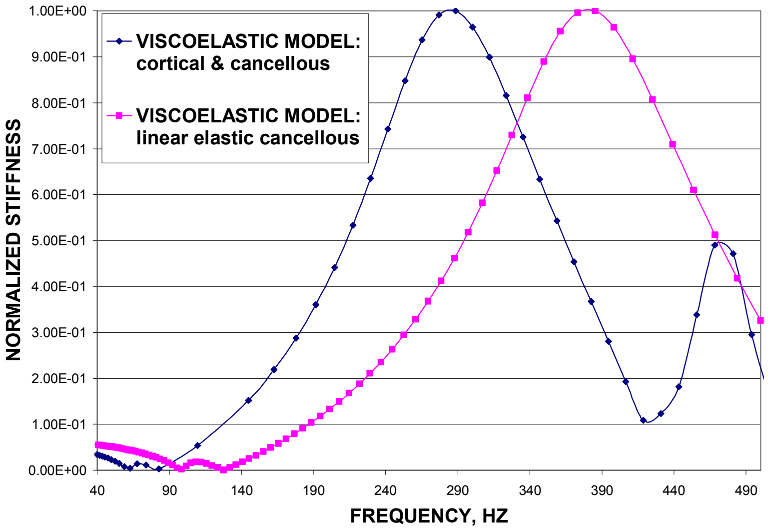

Figure D.1: Effects of adding viscoelastic behavior to cancellous bone

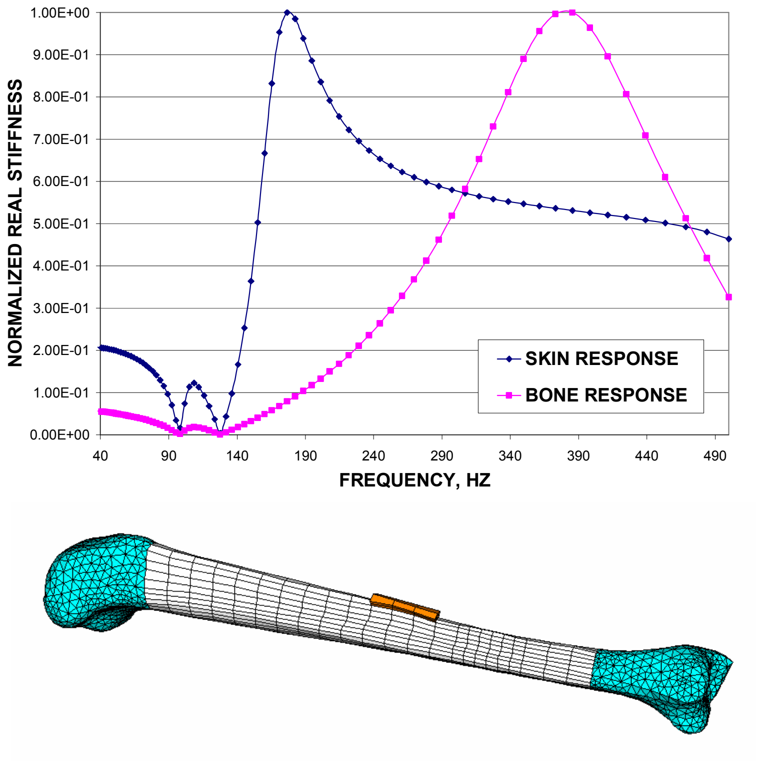

Figure D.2: Skin layer effects between tibia and forcing Probe

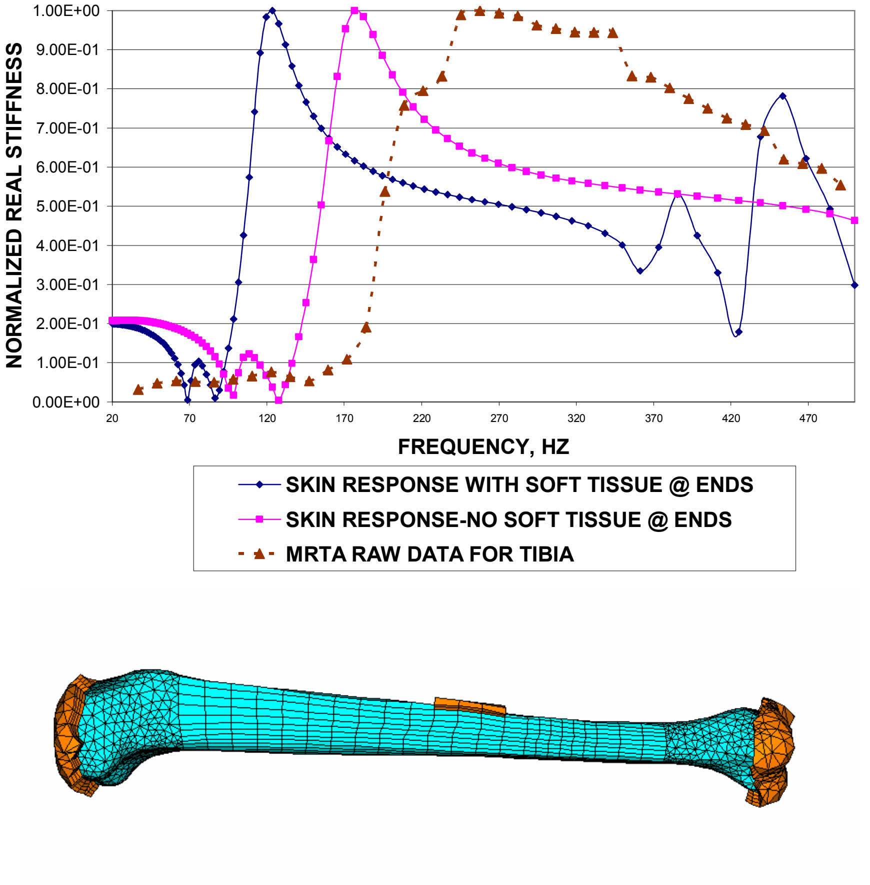

Figure D.3: Effects of soft tissue at the proximal and distal ends

# Vita

Jared Ragone was born in Easton, Pennsylvania on December 3, 1981, but grew up in Spartanburg, South Carolina. He graduated from Spartanburg High School with keen interests in biology, mathematics, and sports medicine after having ACL reconstruction from a soccer-related injury. He is one of five members of the Ragone family (third generation) to attend Virginia Polytechnic Institute and State University. He was a member of the Virginia Tech varsity men's soccer team until his sophomore year when he decided to concentrate on a degree in engineering. In May of 2004, he graduated from Virginia Tech with a B.S. in Engineering Science and Mechanics, a minor in Mathematics, and an option in Biomechanics. After a senior design project related to bone biomechanics, Jared decided to pursue a Master's degree in biomedical engineering at the Virginia Tech-Wake Forest School of Biomedical Engineering and Sciences. Upon completion of this degree, he plans on entering the workforce but still supports the possibility of continuing his education in pursuit of a Doctoral degree.